Supporting Information

Aggregation-Induced Emission Active Donor-Acceptor Fluorophore as a Dual Sensor for Volatile Acids and Aromatic Amines

Kingshuk Debsharma,[†] *Jampani Santhi,*[†] *Beeraiah Baire,**[,†] *and Edamana Prasad**[,†]

[†]Department of Chemistry, Indian Institute of Technology Madras (IIT M), Chennai 600 036, India

Corresponding Authors' Email Address: beeru@iitm.ac.in (B.B.).

edamana20@gmail.com (E.P.).

Experimental Methods:

Synthetic strategy for preparation of indeno[1,2-*c*]pyrroles:

The desired indeno-pyrrole derivative, namely 2-Benzyl-1-(4-methoxyphenyl)-3-phenylindeno[1,2-*c*]pyrrol-8(2*H*)-one (PYROMe) with tethered benzyl, methoxy phenyl and phenyl groups was synthesized based a modified procedure, published by Baire et al.[1] An *N*-iodosuccinimide (NIS) nurtured transition metal free reaction cascade was utilized for rapid generation of PYROMe from the enaminone-alkyne (1) substrate *via* [3+2] cycloaddition reaction (Scheme S1):

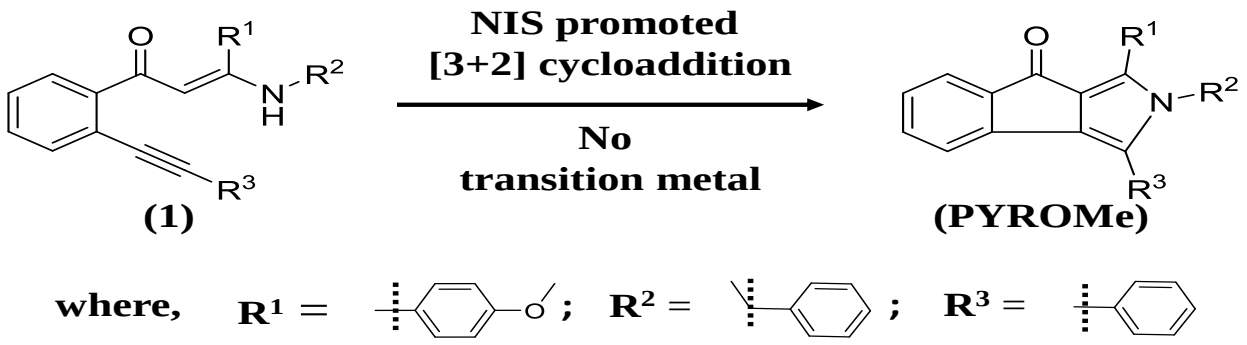

Scheme S1. Synthetic approach for preparation of indeno[1,2-*c*]pyrroles.

UV-visible absorption studies:

The UV-visible absorption measurement was performed in a JASCO V-760 spectrophotometer under room temperature using two faced transparent squared faced quartz cuvettes having path length equalled to 1 cm. For solution state measurement, concentration of the probe was kept at 10 μM and the analyte concentrations were varied equivalently. For solid state measurement, a drop-casted thin film, fabricated on a filter paper was utilized in the same instrument.

Steady-state photoluminescence studies:

The steady-state photoluminescence experiments were executed in a Horiba Jobin Yvon Fluoromax-4 using four faced transparent squared shaped quartz cuvette under room temperature. Likewise absorption studies, concentration of the probe was kept at 10 μM throughout the solution state measurement, while analyte concentrations were varied equivalently. For solid state measurement, same instrument was utilized with different instrumental set up. During both solution and solid state measurements, excitation/emission slit widths were fixed as 2/2.

Time resolved luminescence decay measurements:

A Horiba Jobin Yvon Fluorocube instrument with a TCSPC alignment was employed for the time resolved luminescence decay measurement. A diode laser (λ_{ex} = 370 nm) was used as an excitation source, having a pulse repetition rate of 1 MHz. The instrumental response function (IRF) for λ_{ex} was 1.28 ns and the lamp profile was recorded using a scatterer (Ludox AS40, colloidal silica, Sigma Aldrich) in water. The fluorescence decay profiles were collected near to the respective emission maxima, followed by its analysis with IBH DAS6 software in accordance to the following equation:

$$I(t) = \sum A_i e^{-\frac{t}{\tau_i}}$$

Where, τ_i is the luminescence lifetime of i^{th} species and A_i represents the amplitude of the corresponding decay. The decay profiles of PYROMe in different solvents as well as in THF/H_2O mixture at higher water fraction were fitted biexponentially. During fitting, χ^2 values were adjusted within the valid range.

Measurement of absolute fluorescence quantum yield:

A calibrated integrating sphere was utilized for measurement of absolute quantum yield [ϕ_f (%)] of PYROMe in THF/H_2O mixtures and in solid state. The working principle is based on the following equation:

$$\phi = \frac{N_{em}}{N_{ab}} = \frac{\alpha \int \frac{\lambda}{hc} I_{em}(\lambda) d\lambda}{\alpha \int \frac{\lambda}{hc} [I_{ex}(\lambda) - I'_{ex}(\lambda)] d\lambda}$$

Where, N_{em} and N_{ab} are the respective numbers of emitted and absorbed photons, α is the calibration factor for measurements, h, c, $I_{em}(\lambda)$ are Plank's constant, velocity of light and the intensity of emitted photons at λ. Corresponding $I_{ex}(\lambda)$, $I'_{ex}(\lambda)$ are intensities of excited laser beams in absence and in presence of the sample respectively.

Preparation of nanoaggregates:

Nanoaggregates of PYROMe were prepared by injecting small aliquot (50 µL) of stock solution (1mM) into THF followed by increased volume fraction of added water with vigorous stirring. The final concentration of fluorophore in the binary solvent mixture was adjusted in micromolar (µM) regime.

Dynamic light scattering (DLS) experiments:

The size distribution of the evolved aggregates in THF at higher water fraction was determined through DLS experiment, using Malvern Zetasizer Nano-ZS90 instrument. A transparent quartz cuvette with a path length equalled to 1 cm, containing the desired solution of appropriate height (minimum 10 nm to maximum 15 nm) was utilized in the experiment. A 632.8 nm laser was employed as an excitation source at a fixed scattering angle (90˚).

Morphology:

Scanning electron microscope (SEM) images of PYROMe aggregates, developed on ITO substrates were recorded using FE-SEM instrument (Model: HITACHI S 4800). Before recording the images, the sample was subjected to gold sputter coating for 60 seconds using HITACHI E-1010 ion sputter. The desired aggregates were prepared by fine drop-casting a small proportion (~3 µL) of the diluted PYROMe solution in THF (10 µM) on the ITO substrate followed by drying in vacuum for overnight. To monitor the variation in aggregated morphology in presence of gaseous analytes, sample coated ITO plates were allowed to keep in closed containers consecutively, filled with saturated acid (TFA) and amine (TEA) vapors for 15 and 45 minutes, before recording the respective images without any further time lag.

Cyclic Voltammetry (CV):

The CV measurements of PYROMe in ACN (1 mM) were performed on a CH 660A electrochemical work station (CH Instruments, USA). To record the cyclic voltammogram, a Platinum electrode (3 mm in diameter), a saturated Ag/AgCl electrode, and a platinum wire electrode were chosen as working (W.E.), reference (R.E.) and counter (C.E.) electrodes respectively in the three electrode system. From the onset oxidation potential, HOMO energy level of PYROMe was calculated based on following equation:[2]

$$HOMO\ (eV) = -\left(E_{ox}^{onset} - E_{Fc+/Fc}^{onset}\right) - 4.8$$

Measurement technique of sensory responses for portable thin film:

The fabricated thin film of PYROMe was placed in a sealed quartz container followed by successive injection of increased volume of saturated vapor into the container. The different gaseous concentrations of the desired analytes could be obtained from the following equation:

$$c\ (ppm) = \frac{P_S \times V_S \times 10^6}{V_C \times P}$$

where, V_S and V_C are the analyte (vapor) volume and container volume, respectively; P_S and P represent saturated vapor pressure of the analyte and the atmospheric pressure respectively.

Computational details:

The full geometry optimization of PYROMe was performed with Becke's three-parameters hybrid method (B3LYP) in term of density functional theory (DFT), taking into account the polarizable continuum model (PCM).[3] The triple split valance basis set, viz. 6-311(++)G(d,p), including a set of d-type and p-type polarization functions for all non-hydrogen and hydrogen atoms were deployed for the calculations with additional diffused function. The geometry optimizations were performed with respect to all geometrical variables, regardless of any geometrical constrains. Subsequently, absence of any imaginary frequencies confirmed that the geometries were optimized at their respective energy minima. In order to achieve the simulated absorption spectrum with plausible assignment of the obtained absorption peaks, excitation energies were computed using TDDFT/B3LYP/6-311(++)G(d,p) level of theory,[4] operated on the optimized geometry of PYROMe.

Single crystal XRD study:

Table S1. Crystal data and structure refinement for PYROMe **(**The CCDC **1939748** contains the supplementary crystallographic data for this paper. These data can be obtained free of charge from The Cambridge Crystallographic Data Centre**)**

Identification code	PYROME	
Empirical formula	C31 H23 N O2	
Formula weight	441.50	
Temperature	296(2) K	
Wavelength	0.71073 Å	
Crystal system	Monoclinic	
Space group	$P2_1/c$	
Unit cell dimensions	a = 10.5237(8) Å	α= 90°.
	b = 23.6656(18) Å	β= 93.783(2)°.
	c = 9.4068(6) Å	γ = 90°.
Volume	2337.7(3) $Å^3$	
Z	4	
Density (calculated)	1.254 Mg/m^3	
Absorption coefficient	0.078 mm^{-1}	
F(000)	928	
Crystal size	0.300 x 0.250 x 0.200 mm^3	
Theta range for data collection	3.126 to 24.999°.	
Index ranges	-12<=h<=12, -28<=k<=28, -11<=l<=10	
Reflections collected	37232	
Independent reflections	4106 [R(int) = 0.0803]	
Completeness to theta = 24.999°	99.7 %	
Absorption correction	Semi-empirical from equivalents	
Max. and min. transmission	0.7452 and 0.7254	
Refinement method	Full-matrix least-squares on F^2	
Data / restraints / parameters	4106 / 0 / 308	
Goodness-of-fit on F^2	1.043	
Final R indices [I>2sigma(I)]	R1 = 0.0524, wR2 = 0.1101	
R indices (all data)	R1 = 0.0992, wR2 = 0.1305	
Extinction coefficient	n/a	
Largest diff. peak and hole	0.146 and -0.215 $e.Å^{-3}$	

Table S2. Torsion angles [°] for PYROMe

C(6)-C(1)-C(2)-C(3)	-0.9(4)
C(1)-C(2)-C(3)-C(4)	0.0(4)
C(2)-C(3)-C(4)-C(5)	0.7(4)
C(3)-C(4)-C(5)-C(6)	-0.5(3)

C(3)-C(4)-C(5)-C(9)	177.4(2)
C(2)-C(1)-C(6)-C(5)	1.1(3)
C(2)-C(1)-C(6)-C(7)	-177.0(2)
C(4)-C(5)-C(6)-C(1)	-0.4(3)
C(9)-C(5)-C(6)-C(1)	-178.63(19)
C(4)-C(5)-C(6)-C(7)	178.2(2)
C(9)-C(5)-C(6)-C(7)	-0.1(2)
C(1)-C(6)-C(7)-C(10)	-1.2(5)
C(5)-C(6)-C(7)-C(10)	-179.5(3)
C(1)-C(6)-C(7)-C(8)	178.4(2)
C(5)-C(6)-C(7)-C(8)	0.1(2)
C(10)-C(7)-C(8)-C(11)	0.1(2)
C(6)-C(7)-C(8)-C(11)	-179.65(17)
C(10)-C(7)-C(8)-C(9)	179.67(17)
C(6)-C(7)-C(8)-C(9)	0.0(2)
C(11)-C(8)-C(9)-O(1)	-0.9(5)
C(7)-C(8)-C(9)-O(1)	179.7(2)
C(11)-C(8)-C(9)-C(5)	179.4(3)
C(7)-C(8)-C(9)-C(5)	0.0(2)
C(4)-C(5)-C(9)-O(1)	2.2(4)
C(6)-C(5)-C(9)-O(1)	-179.7(2)
C(4)-C(5)-C(9)-C(8)	-178.1(2)
C(6)-C(5)-C(9)-C(8)	0.0(2)
C(8)-C(7)-C(10)-N(1)	-0.7(2)
C(6)-C(7)-C(10)-N(1)	178.9(3)
C(8)-C(7)-C(10)-C(26)	174.6(2)
C(6)-C(7)-C(10)-C(26)	-5.9(5)
C(7)-C(8)-C(11)-N(1)	0.6(2)
C(9)-C(8)-C(11)-N(1)	-178.8(3)
C(7)-C(8)-C(11)-C(12)	-174.02(19)
C(9)-C(8)-C(11)-C(12)	6.6(4)
N(1)-C(11)-C(12)-C(13)	-146.5(2)
C(8)-C(11)-C(12)-C(13)	27.1(3)
N(1)-C(11)-C(12)-C(17)	34.0(3)
C(8)-C(11)-C(12)-C(17)	-152.3(2)
C(17)-C(12)-C(13)-C(14)	-3.3(3)
C(11)-C(12)-C(13)-C(14)	177.2(2)
C(12)-C(13)-C(14)-C(15)	0.5(3)
C(13)-C(14)-C(15)-O(2)	-177.1(2)
C(13)-C(14)-C(15)-C(16)	2.6(3)

O(2)-C(15)-C(16)-C(17)	176.9(2)
C(14)-C(15)-C(16)-C(17)	-2.8(3)
C(15)-C(16)-C(17)-C(12)	-0.1(3)
C(13)-C(12)-C(17)-C(16)	3.1(3)
C(11)-C(12)-C(17)-C(16)	-177.5(2)
N(1)-C(19)-C(20)-C(21)	-10.2(3)
N(1)-C(19)-C(20)-C(25)	168.15(19)
C(25)-C(20)-C(21)-C(22)	0.7(4)
C(19)-C(20)-C(21)-C(22)	179.1(2)
C(20)-C(21)-C(22)-C(23)	-0.8(4)
C(21)-C(22)-C(23)-C(24)	0.4(4)
C(22)-C(23)-C(24)-C(25)	0.2(4)
C(23)-C(24)-C(25)-C(20)	-0.3(4)
C(21)-C(20)-C(25)-C(24)	-0.1(3)
C(19)-C(20)-C(25)-C(24)	-178.6(2)
C(7)-C(10)-C(26)-C(27)	-71.6(3)
N(1)-C(10)-C(26)-C(27)	103.1(3)
C(7)-C(10)-C(26)-C(31)	107.6(3)
N(1)-C(10)-C(26)-C(31)	-77.7(3)
C(31)-C(26)-C(27)-C(28)	1.7(4)
C(10)-C(26)-C(27)-C(28)	-179.1(3)
C(26)-C(27)-C(28)-C(29)	-0.9(5)
C(27)-C(28)-C(29)-C(30)	0.5(5)
C(28)-C(29)-C(30)-C(31)	-0.8(5)
C(27)-C(26)-C(31)-C(30)	-2.0(4)
C(10)-C(26)-C(31)-C(30)	178.8(3)
C(29)-C(30)-C(31)-C(26)	1.6(5)
C(8)-C(11)-N(1)-C(10)	-1.0(2)
C(12)-C(11)-N(1)-C(10)	173.82(18)
C(8)-C(11)-N(1)-C(19)	-175.43(18)
C(12)-C(11)-N(1)-C(19)	-0.6(3)
C(7)-C(10)-N(1)-C(11)	1.1(2)
C(26)-C(10)-N(1)-C(11)	-174.69(19)
C(7)-C(10)-N(1)-C(19)	175.68(18)
C(26)-C(10)-N(1)-C(19)	-0.1(3)
C(20)-C(19)-N(1)-C(11)	-88.4(2)
C(20)-C(19)-N(1)-C(10)	97.9(2)
C(14)-C(15)-O(2)-C(18)	3.6(4)
C(16)-C(15)-O(2)-C(18)	-176.1(3)

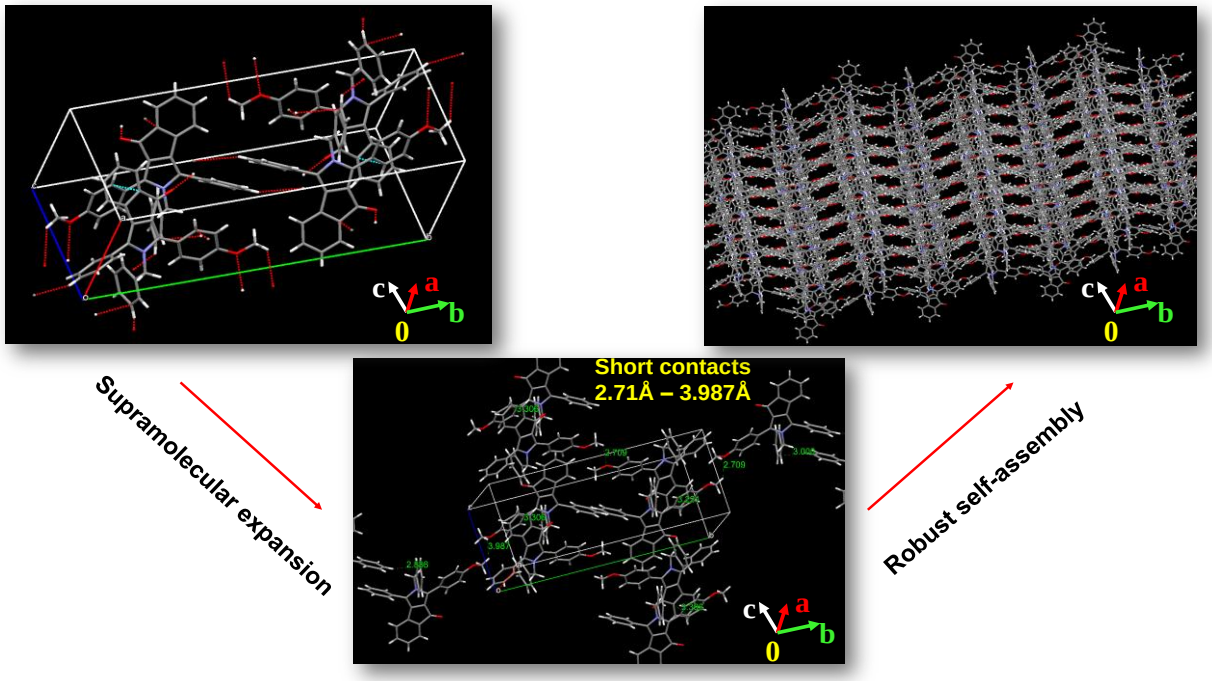

Figure S1. Three dimensional supramolecular propagation of PYROMe, utilizing short intermolecular contacts ranging from 2.71 Å – 3.987 Å.

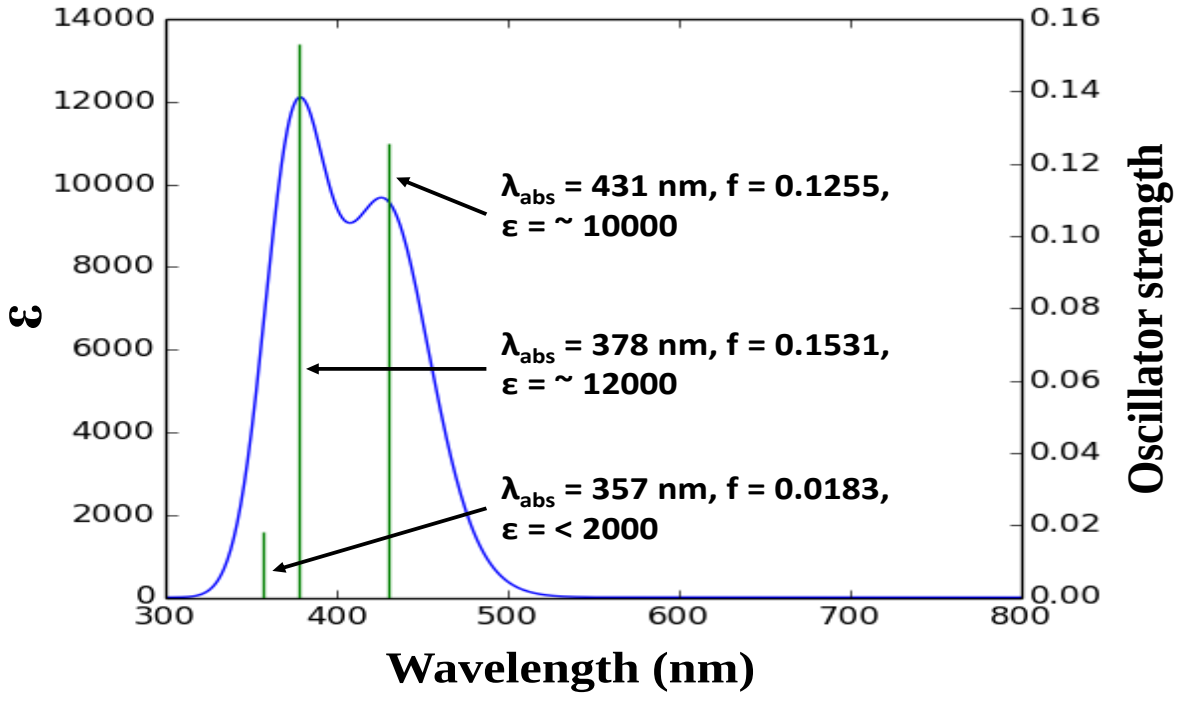

Figure S2. Theoretically obtained absorption spectrum of PYROMe at TD-B3LYP/6-311(++)G(d,p) level of calculation.

Table S3. Simulated absorption parameters of PYROMe, obtained from TD-B3LYP/6-311(++)G(d,p) level of calculation

State	λ (nm)	E_g (eV)	f	Orbital contribution
S_1	431	2.8753	0.1255	HOMO → LUMO (88%) H-1 → LUMO (10%)
S_2	378	3.2727	0.1531	H-1 → LUMO (85%) H-3 → LUMO (2%) HOMO → LUMO (9%)
S_3	357	3.4662	0.0183	H-3 → LUMO (80%) H-4 → LUMO (8%) H-8 → LUMO (4%)

Table S4. The CIE coordinates of PYROMe in different solvents

Solvents	CIE coordinates
MCH	(0.16, 0.29)
TOL	(0.20, 0.35)
THF	(0.22, 0.48)
DCM	(0.28, 0.53)
DMF	(0.27, 0.54)
DMSO	(0.31, 0.56)

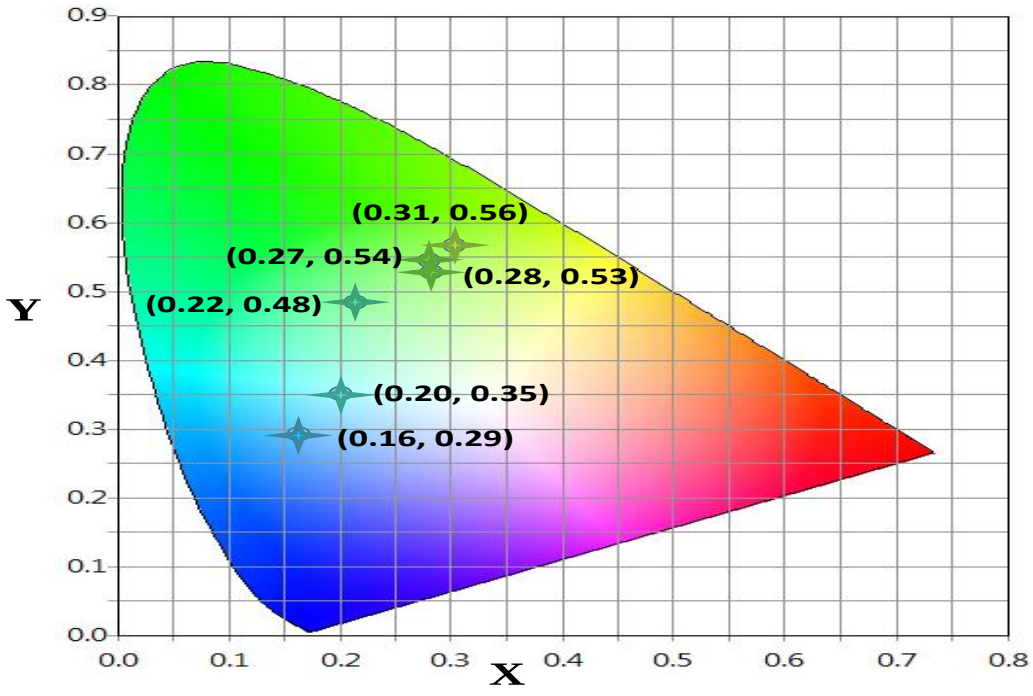

Figure S3. The CIE graph of PYROMe in different solvents.

Table S5. Lippert-Mataga parameters of PYROMe

Solvent	Δf	Stokes shift (cm^{-1})
MCH	-5.8×10^{-4}	7910.27
TOL	0.0131	7967.00
THF	0.1996	8769.45
DCM	0.2094	8847.56
DMF	0.2170	9011.92
DMSO	0.2744	9353.30

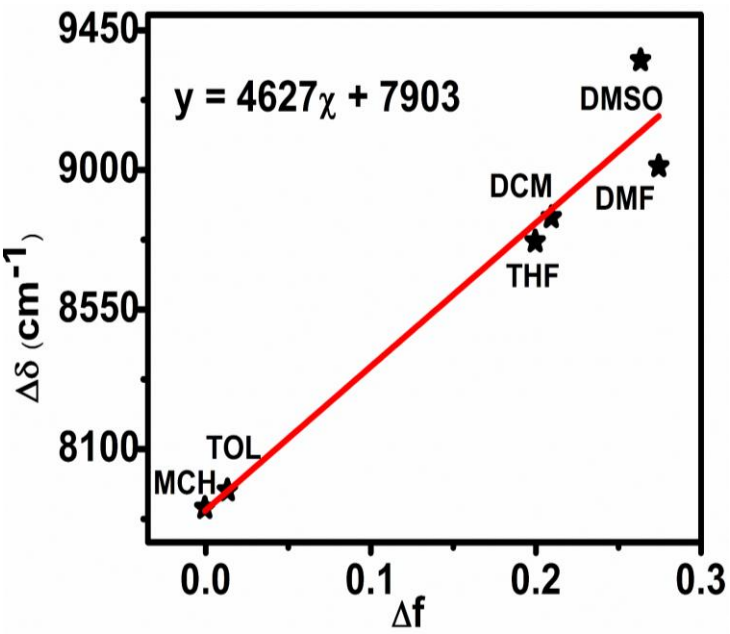

Figure S4. Plot of Stokes shift (Δδ) of PYROMe versus orientation polarizability (Δf).

Calculation of dipole moment change of PYROMe using Lippert-Mataga equation:

The change in dipole moment of PYROMe from ground state to excited state was calculated using Lippert-Mataga equation,[5] taking into account the positive slope of Stokes shift versus orientation polarizability plot (Figure S4). The orientational polarizability (Δf) is described by following equation:

$$\Delta f(\epsilon,\eta) = \left(\frac{\epsilon-1}{2\epsilon+1} - \frac{\eta^2-1}{2\eta^2+1}\right) \qquad (S1)$$

and the Lippert-Mataga equation is represented as:

$$\delta_A - \delta_F = \Delta\delta = \frac{2}{\mathrm{hc}}\left(\frac{\epsilon-1}{2\epsilon+1} - \frac{\eta^2-1}{2\eta^2+1}\right)\frac{(\mu_E-\mu_G)^2}{a^3} + constant \qquad (S2)$$

where, $\delta_A - \delta_F$ i.e. $\Delta\delta$ represents difference between absorption and emission maxima in wave numbers. $\mu_E - \mu_G$ is the difference between excited and ground state dipole moments. h, c, ϵ, η and a are Planck constant, velocity of light, static dielectric constant, optical refractive index and Onsager solvent cavity radius respectively.

According to the Lippert-Mataga equation, slope can be represented as follows:

$$Slope = \frac{2}{hc}\frac{(\mu_E-\mu_G)^2}{a^3} \qquad (S3)$$

Rearranging the eq. S3 we have:

$$(\mu_E - \mu_G) = \sqrt{[0.5hca^3(slope)]} \qquad (S4)$$

The magnitudes of Planck constant (h), velocity of light (c), Onsager's solvent cavity radius (a) and slope were taken as follows:

h = 6.626×10^{-27} erg s; c = 3×10^{10} cms^{-1}; a = 10.589 Å (from the crystal structure of PYROMe) and slope = 4627 cm^{-1}.

Putting those values in eq. S4, magnitude of (μ_E - μ_G) was found to be 23.37 D.

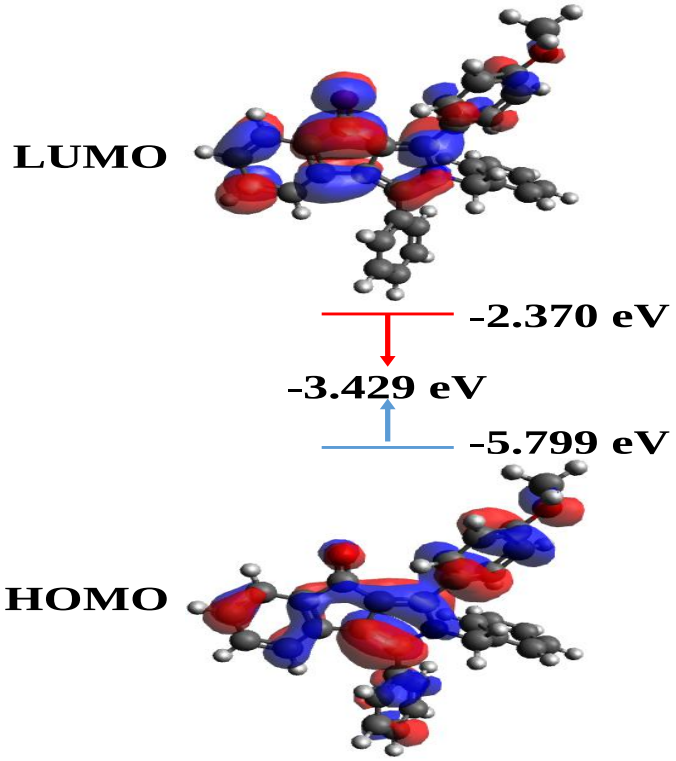

Figure S5. The spatial FMOs (HOMO and LUMO) of PYROMe under its respective optimized geometry in DMSO exhibit the heterogeneous electron distribution from indeno-pyrrole ring, methoxy phenyl and phenyl groups in HOMO to carbonyl group in LUMO. The desired optimization was carried out using B3LYP/6-311(++)G(d,p) level of theory at PCM model in Gaussian 09 suite of programme.

Table S6. The HOMO-LUMO energy gaps of PYROMe in different solvents

Solvent	$-\Delta E_{HOMO-LUMO}$ (eV)
MCH	3.489
TOL	3.481
THF	3.443
DCM	3.440
DMF	3.430
DMSO	3.429

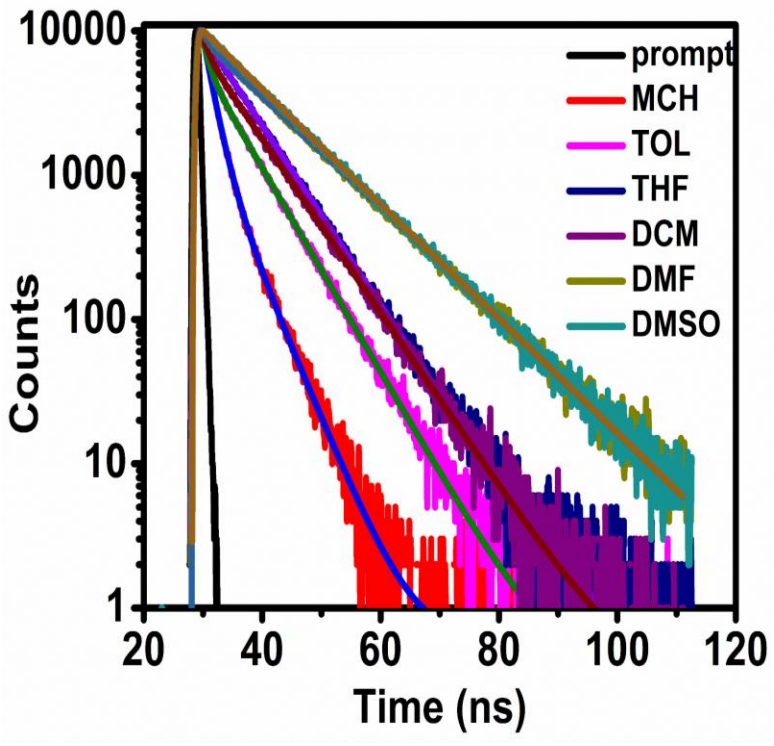

Figure S6. Time resolved fluorescence decay profile of PYROMe in different solvents (λ_{ex} = 370 nm)

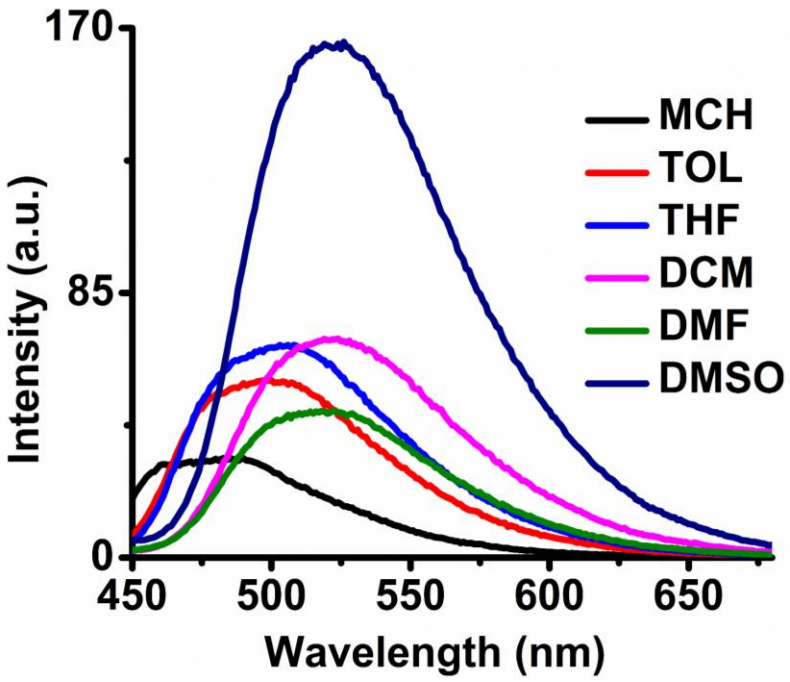

Figure S7. Emission spectra of PYROMe in different solvents (λ_{ex} = 350 nm, concentration = 10 μM).

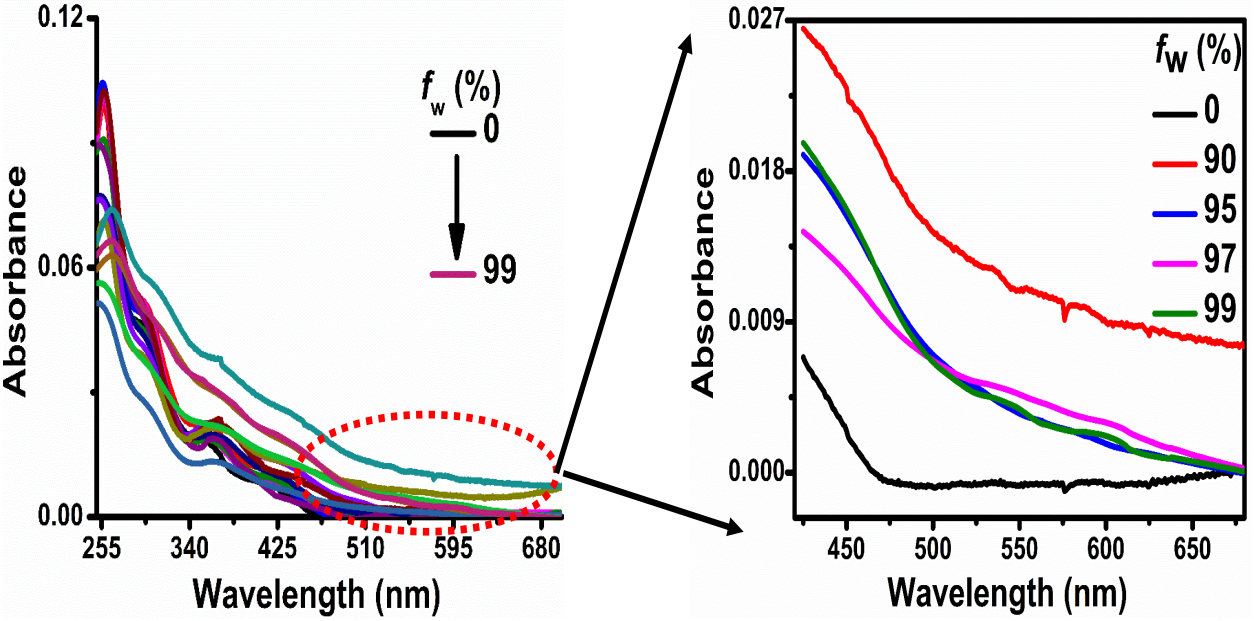

Figure S8. Absorption spectra of PYROMe in THF with increased f_w (%) (left) exhibit the level of tailing in higher f_w (%) at longer wavelength region (right) (concentration = 10 μM).

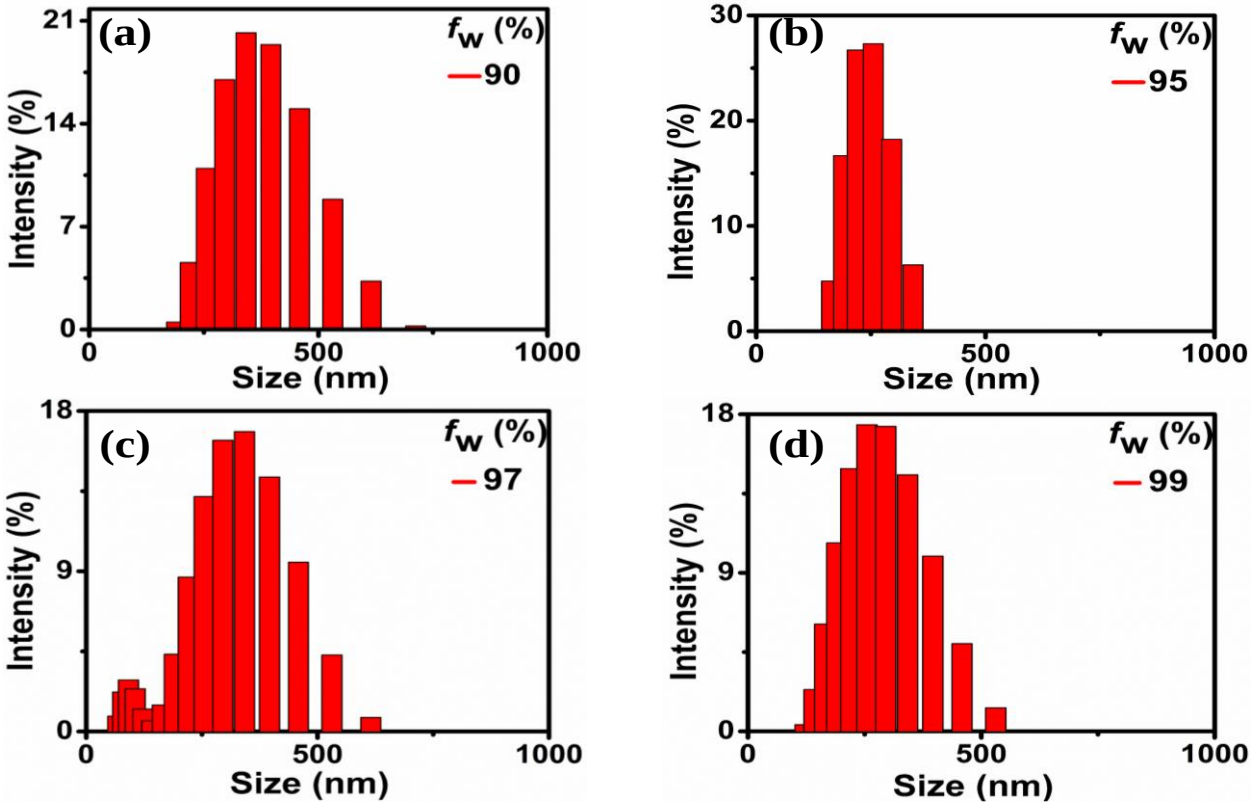

Figure S9. DLS traces of PYROMe in THF/H_2O mixtures at f_w = (a) 90%, (b) 95%, (c) 97% and (d) 99% (concentration = 10 μM).

Table S7. DLS parameters of PYROMe in THF at higher f_w (%) (concentration = 10 μM)

fw (%)	Zavg (nm)	PDI	Peak1 mean intensity (nm)	Peak2 mean intensity (nm)	Peak1 area (%)	Peak2 area (%)
90	200	0.28	186.4	0	100	0
95	165.8	0.43	121.7	0	100	0
97	170.6	0.46	164.9	48.4	89.8	10.2
99	168.4	0.49	140.8	0	100	0

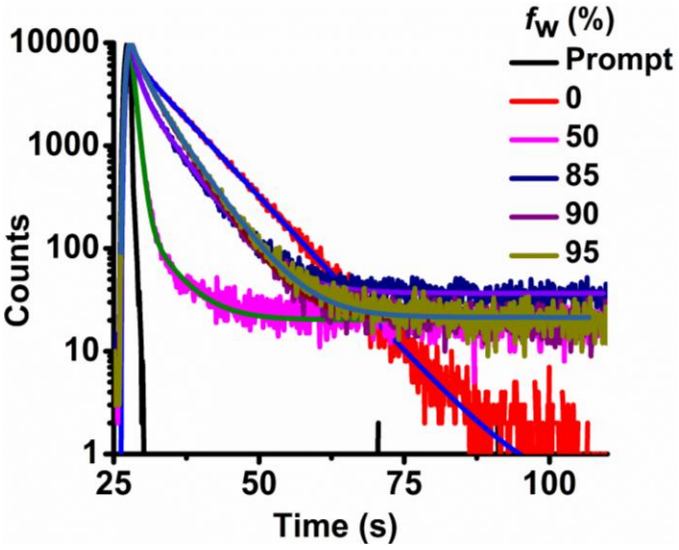

Figure S10. Time resolved fluorescence decay profile of PYROMe in THF/H_2O mixtures at varied f_w (%) (concentration = 10 μM).

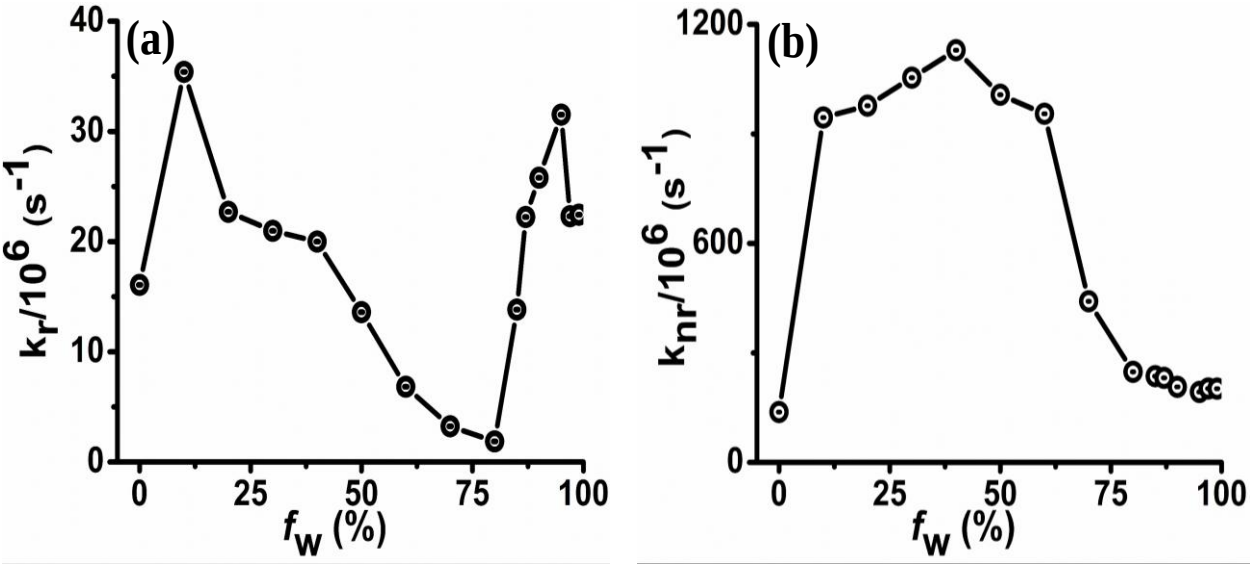

Figure S11. Variation in (a) k_r and (b) k_{nr} of PYROMe in THF with increased f_w (%) (concentration = 10 μM).

Table S8. Time resolved fluorescence decay parameters of PYROMe in THF/H_2O mixtures at varied f_w (%) (concentration = 10 μM)

f_w (%)	τ_1 (ns)	B_1	τ_2 (ns)	B_2	τ_{avg} (ns) (χ^2)
0	1.04	11.41	7.28	89.59	6.49 (1.05)
50	0.74	93.68	4.64	6.32	0.98 (1.35)
85	1.14	33.40	5.40	66.60	4.00 (1.30)
90	1.84	22.92	5.00	77.08	4.27 (1.11)
95	2.00	26.23	5.33	73.77	4.46 (1.26)

Solid state luminescence characteristics of PYROMe

Interestingly it was observed that, emission spectra of PYROMe in as synthesized powder and crystals exhibited a striking resemblance with that in THF/H_2O mixture (f_w = 95%) (Figure S12).

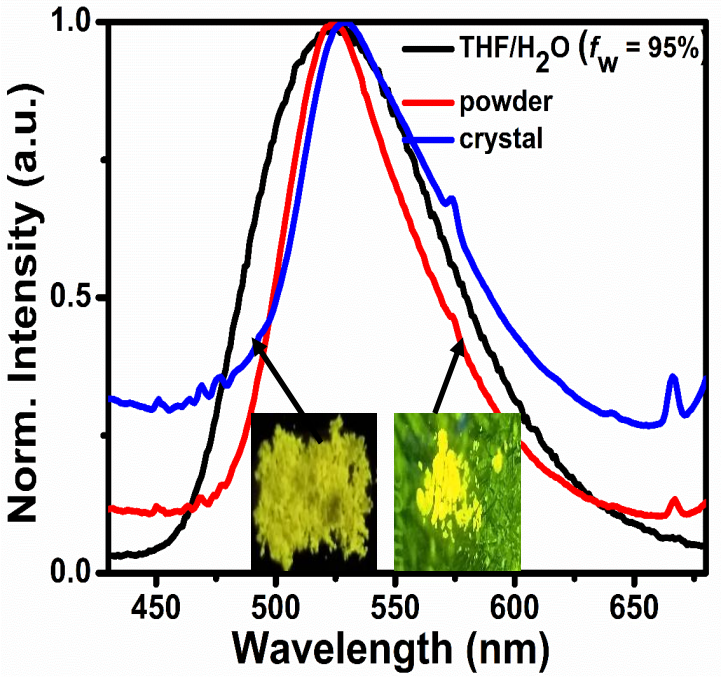

Figure S12. Normalized emission spectra of PYROMe in THF/H_2O (f_w = 95%; concentration = 10 μM), as synthesized powder and crystal form (λ_{ex} = 350 nm). Inset represents the photographs of PYROMe crystal (left) and as synthesized powder (right), excited under UV light (λ_{ex} = 365 nm).

Hence, it can be suggested that, the emission signals from the solid states were also stem from the AIE characteristics. Accordingly, PYROMe displayed efficient emission in both powder and crystals, upon excitation under UV light (λ_{ex} = 365 nm) (Inset of Figure S12). The similarity in the emissive nature suggests almost similar packing arrangement of PYROMe in binary solvent and solid states.[6] Therefore, to denote the packing arrangement; single crystals of PYROMe were carefully examined.

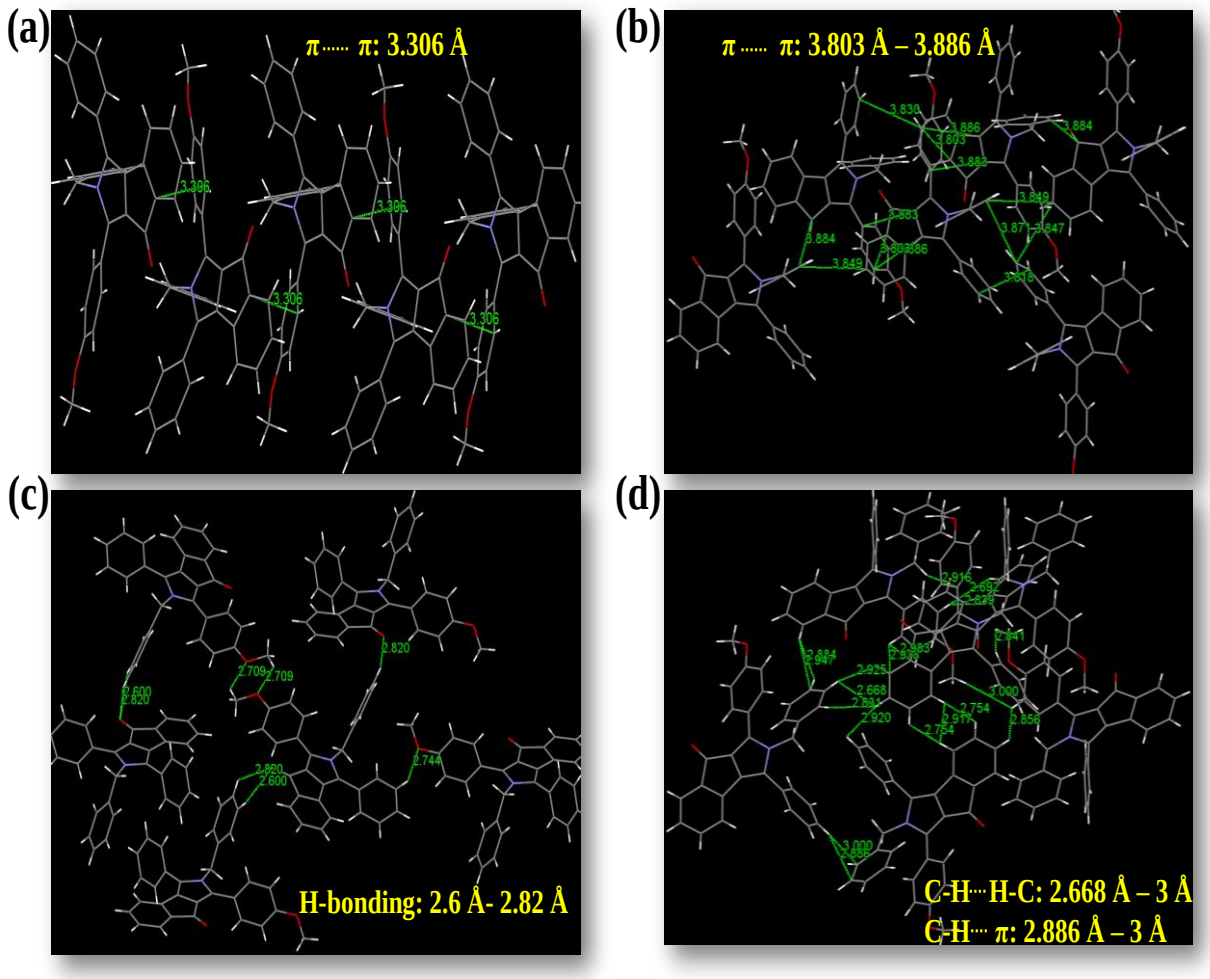

Figure S13. Single crystal structure of PYROMe exhibiting (a, b) intermolecular π ··· π interactions, (c) hydrogen bonding interaction along with several (d) C-H···H-C and C-H···π interactions.

As shown in Figure S13a and b, PYROMe formed two types of intermolecular π ··· π interactions. The strong π ··· π interaction (Figure S13a) was found between substituted methoxy phenyl and central indeno-pyrrole rings (d = 3.306 Å), whereas the weak π ··· π interactions (Figure S13b) were mainly found between (a) indeno-pyrrole and substituted benzyl rings (d = 3.849 Å – 3.884 Å), (b) indeno-pyrrole and phenyl rings (d = 3.847 Å), (c) phenyl and methoxy phenyl substituents (d = 3.830 Å), (d) benzyl and phenyl groups (d = 3.871 Å), (e) two phenyl substituents (d = 3.818 Å) and (f) indeno-pyrrole and substituted methoxy phenyl group (d = 3.803 Å – 3.886 Å). Again three types of intermolecular hydrogen bonding interactions were found between (a) carbonyl group of indeno-pyrrole ring and the hydrogen atoms on substituted benzyl group (d = 2.6 Å – 2.820 Å), (b) oxygen and hydrogen atoms of two methoxy phenyl groups (d = 2.709 Å) and (c) oxygen atom of methoxy phenyl and hydrogen atom of substituted phenyl groups (d = 2.744 Å) in the crystal structure of PYROMe (Figure S13c). Apart from these two classes of interactions, significant number of C-H···H-C interactions (d = 2.668 Å – 3 Å), as well as C-H···π interactions (d = 2.886 Å – 3 Å) were also detected (Figure S13d). These multiple interactions not only stabilized the crystal packing but also induced augmented rigidity within the molecular conformations which could obstruct the energy loss via nonradiative pathways by RIR, enabling PYROMe to retain the luminescence in solid states.[6]

Moreover, during crystal packing, the centroid-to-centroid distance between two PYROMe (Figure S14) was found to be too large (7.049 Å) to form any closed cofacial π···π interaction. As a result PYROMe could successfully rule out any possibility of fluorescence quenching, owing to the formation of excimer and/or exciplex in solid state by hindering the electron delocalization during the course of aggregation.[7]

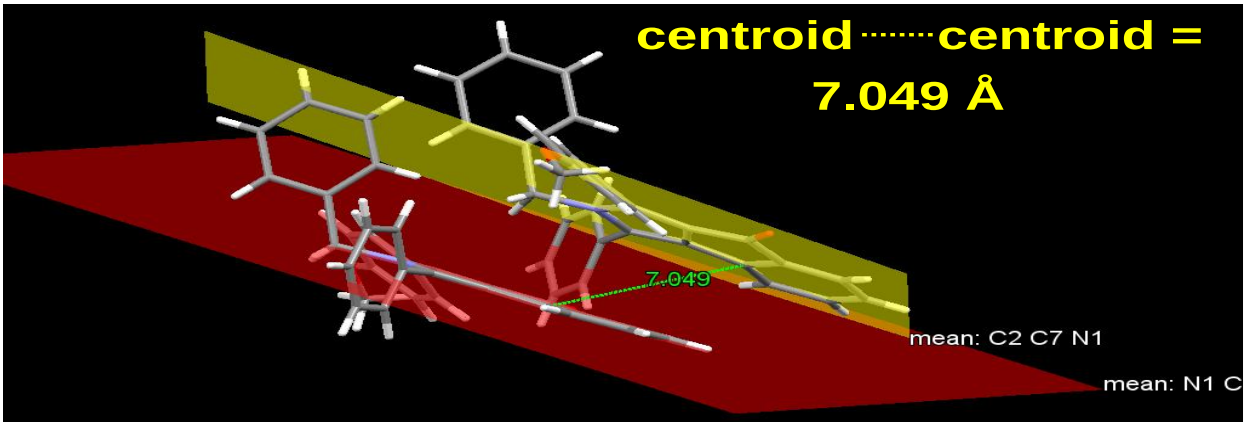

Figure S14. Distance between the centroids of two interplanar PYROMe, obtained from the crystal structure.

Table S9. Quantum yield of PYROMe in THF/H_2O mixture at lower and higher f_w (%)s and in solid powder

THF/H2O		Powder
f_w (%)	[a]ϕ_f (%)	[a]ϕ_f (%)
0	10.85	7.91
50	1.33	
90	8.40	
95	8.47	

[a]ϕ_f were measured using calibrated integrating sphere

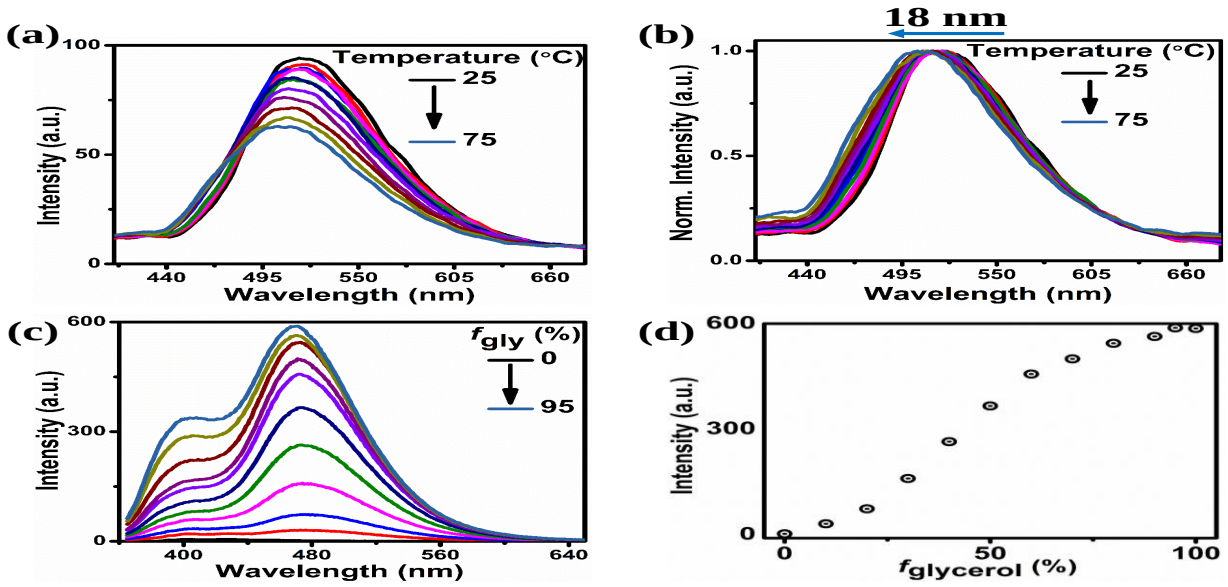

Figure S15. (a) Variation in emission spectra and (b) hypsochromic shift in the peak position of PYROMe in THF/H_2O mixture (f_w = 95%) upon changing temperature from 25 ˚C to 75 ˚C. (c) Alteration in emission spectra and (d) enhancement in the peak intensity at λ_{em} = 470 nm upon increased addition of glycerol fraction ($f_{glycerol}$) in a MeOH solution of PYROMe, containing 1 volume% of THF (λ_{ex} = 350 nm; concentration = 10 μM).

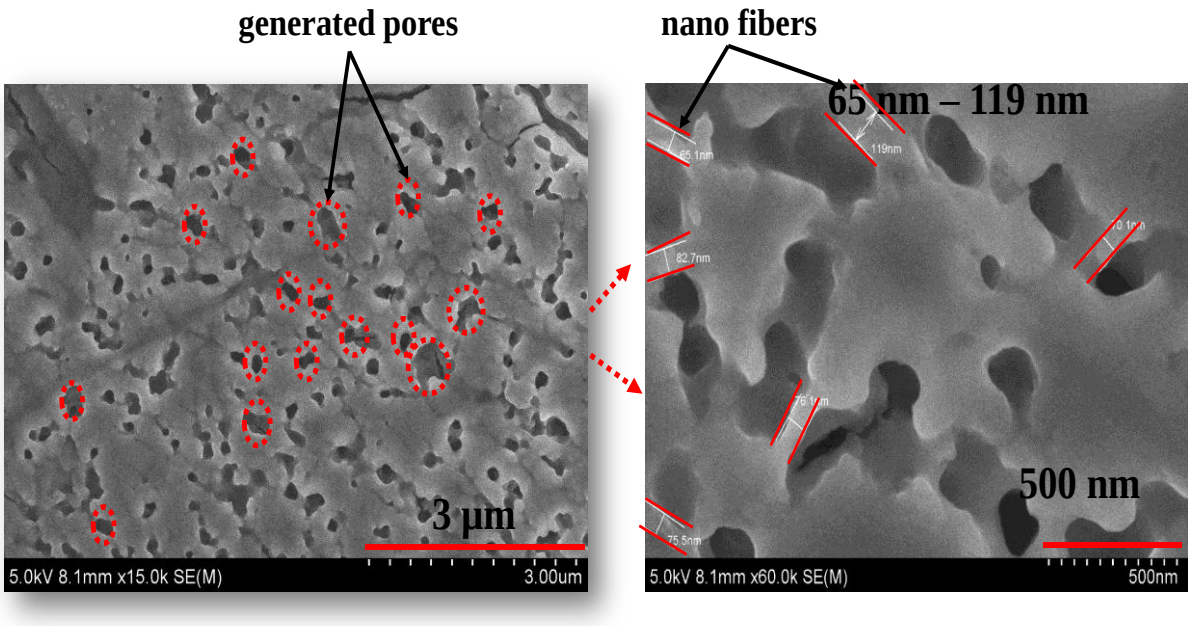

Figure S16. SEM image of the developed film on ITO substrate, revealing existence of entangled porous agglomerated morphology (left). Closed inspection of the obtained porous morphology discloses nanofibrous network, where the diameter of the fibers were ranged between 65 nm to 119 nm (right).

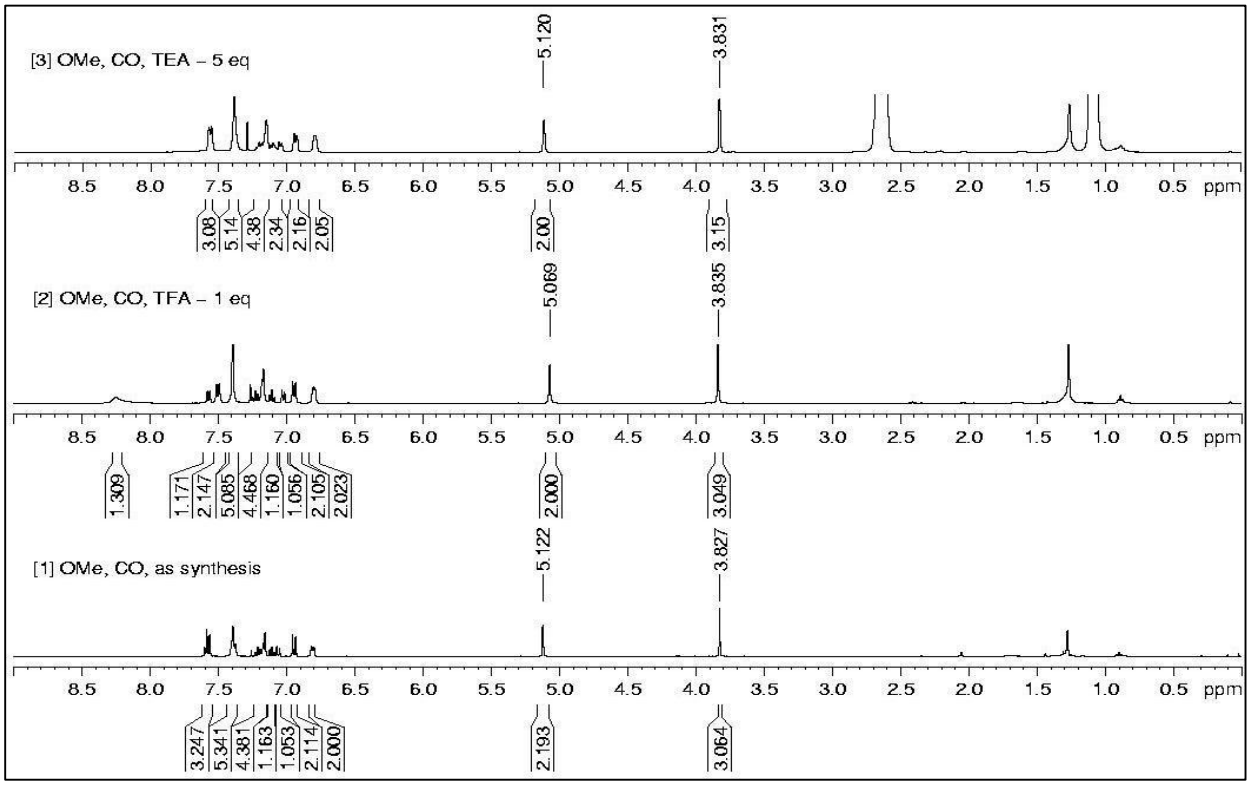

Figure S17. ^{1}H NMR spectra of PYROMe in $CDCl_3$ before (bottom) and after (middle) addition of TFA (1 equiv.) followed by excess (5 equiv.) addition of TEA (top).

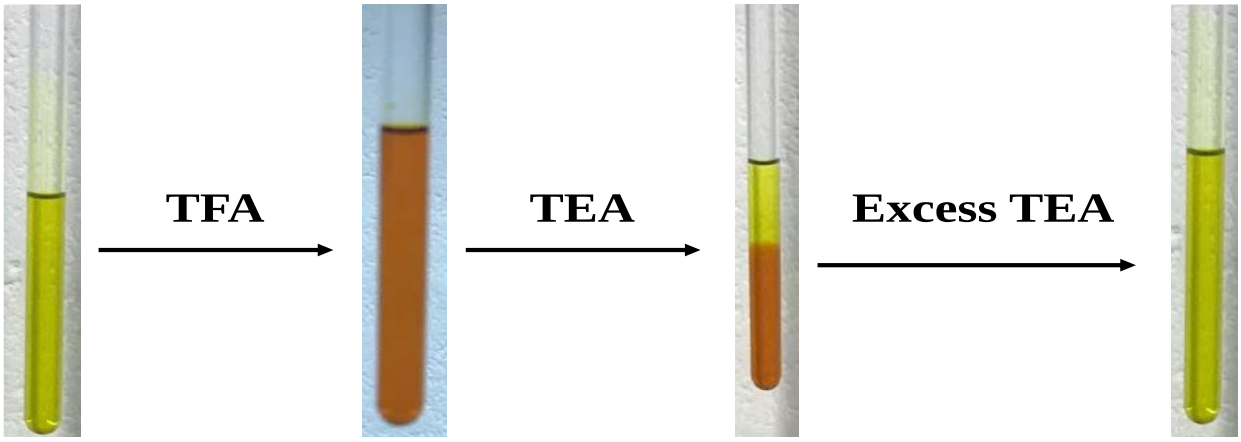

Figure S18. Photographs of $CDCl_3$ solution of PYROMe, taken under normal light, before and after addition of TFA (1 equiv.) followed by excess addition of TEA (5 equiv.).

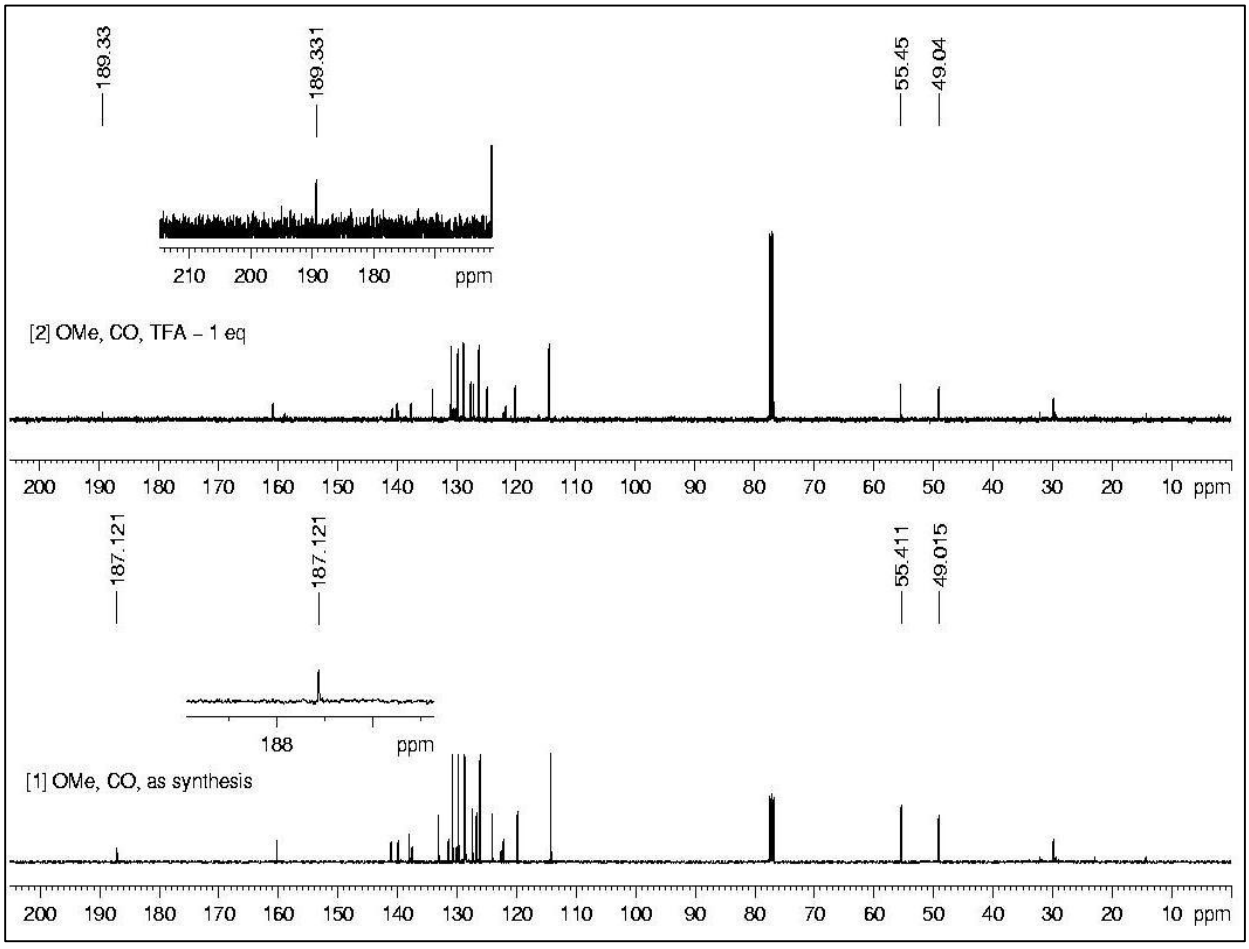

Figure S19. ^{13}C NMR spectra of PYROMe in $CDCl_3$ before (bottom) and after (top) addition of TFA (1 equiv.) illustrates the desired deshielding of carbonyl resonance peak from 187.121 ppm (inset of the bottom spectrum) to 189.331 ppm (inset of the top spectrum).

Synthesis procedure of 2-Benzyl-1-(4-methoxyphenyl)-3-phenyl-2,8-dihydroindeno[1,2-*c*]pyrrole (PYROMe1):

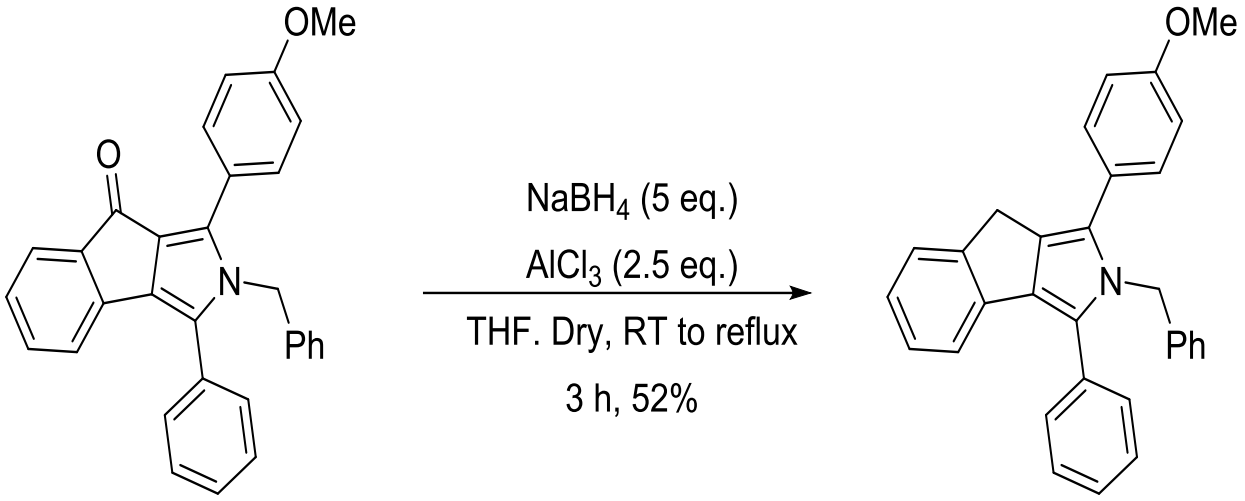

Scheme S2. Represents synthesis procedure of PYROMe1 from the precursor PYROMe.

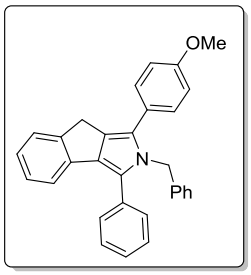

To a solution of PYROMe (80 mg, 0.18 mmol) in anhydrous THF (5 mL), $NaBH_4$ (34 mg, 0.90 mmol) and $AlCl_3$ (60 mg, 0.45 mmol) were added at RT and refluxed for 3 h. Reaction mixture was diluted with water (10 mL), and extracted with ethyl acetate (10 mL). Evaporation of the solvent and purification of the crude reaction mixture by flash chromatography (4:1 hexane: EtOAc) gave the decarbonylated PYROMe1 (40 mg, 0.09 mmol, 52%) as a dark yellow oil.

^{1}H NMR (400 MHz, $CDCl_3$): δ = 7.48 (2 H, d, *J* = 7.1 Hz), 7.43-7.36 (4 H, m), 7.39-7.29 (3 H, m), 7.16-7.06 (5 H, m), 6.89 (2 H, d, *J* = 8.7 Hz), 6.70-6.64 (2 H, m), 5.19 (2 H, s), 3.81 (3 H, s) and 3.76 (2 H, s) ppm.

^{13}C NMR (100 MHz, $CDCl_3$): δ = 158.7, 147.2, 139.5, 138.4, 133.1, 130.2, 129.9, 129.8, 128.6, 128.3, 128.2, 128.0, 127.3, 126.8, 126.6, 126.4, 126.1, 125.9, 125.5, 124.7, 119.5, 114.1, 55.4, 49.1 and 30.9 ppm.

IR (neat): 3055, 2927, 2857, 1606, 1502, 1455, 1253, 1089 and 804 cm^{-1}.

HR ESI-MS: $[C_{31}H_{26}NO]^+ = [M+H]^+$ requires 428.2014; found 428.2024.

TLC: R_f = 0.5 (4:1, HXN/EtOAc).

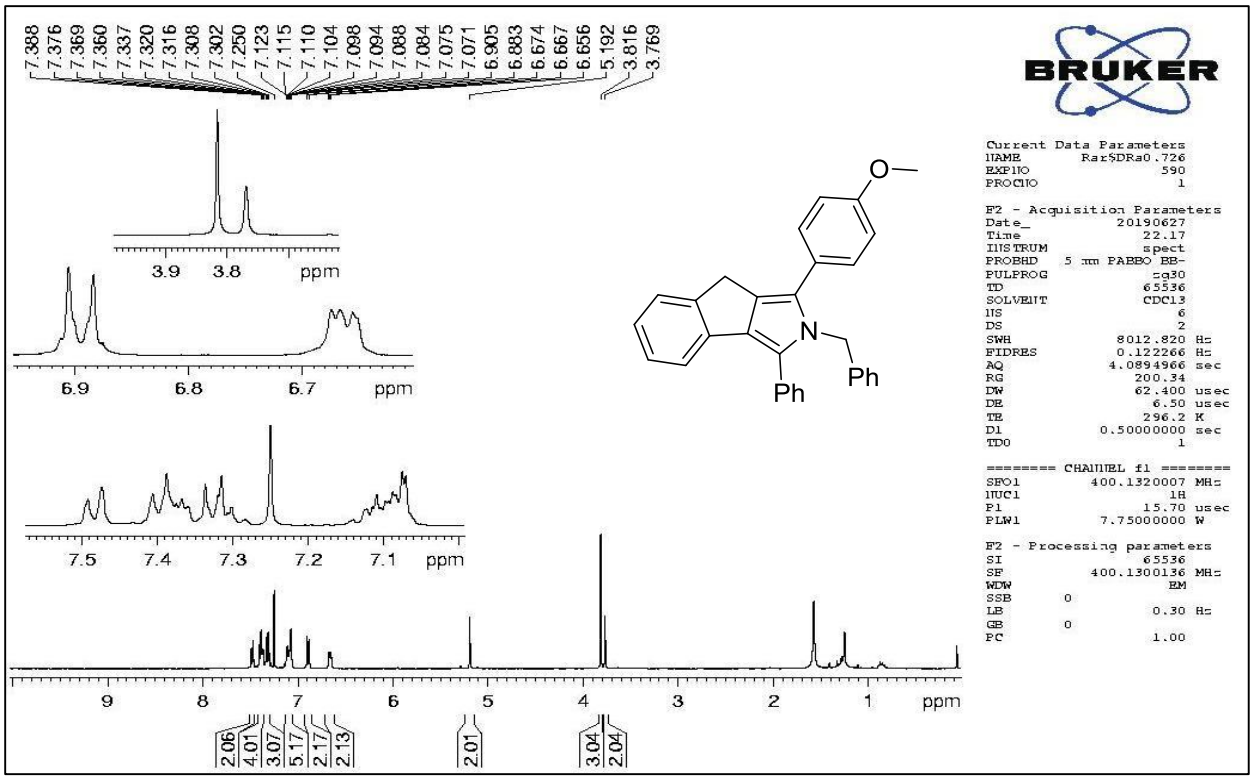

Figure S20. ^{1}H NMR (400 MHz) spectrum of PYROMe1, recorded in $CDCl_3$.

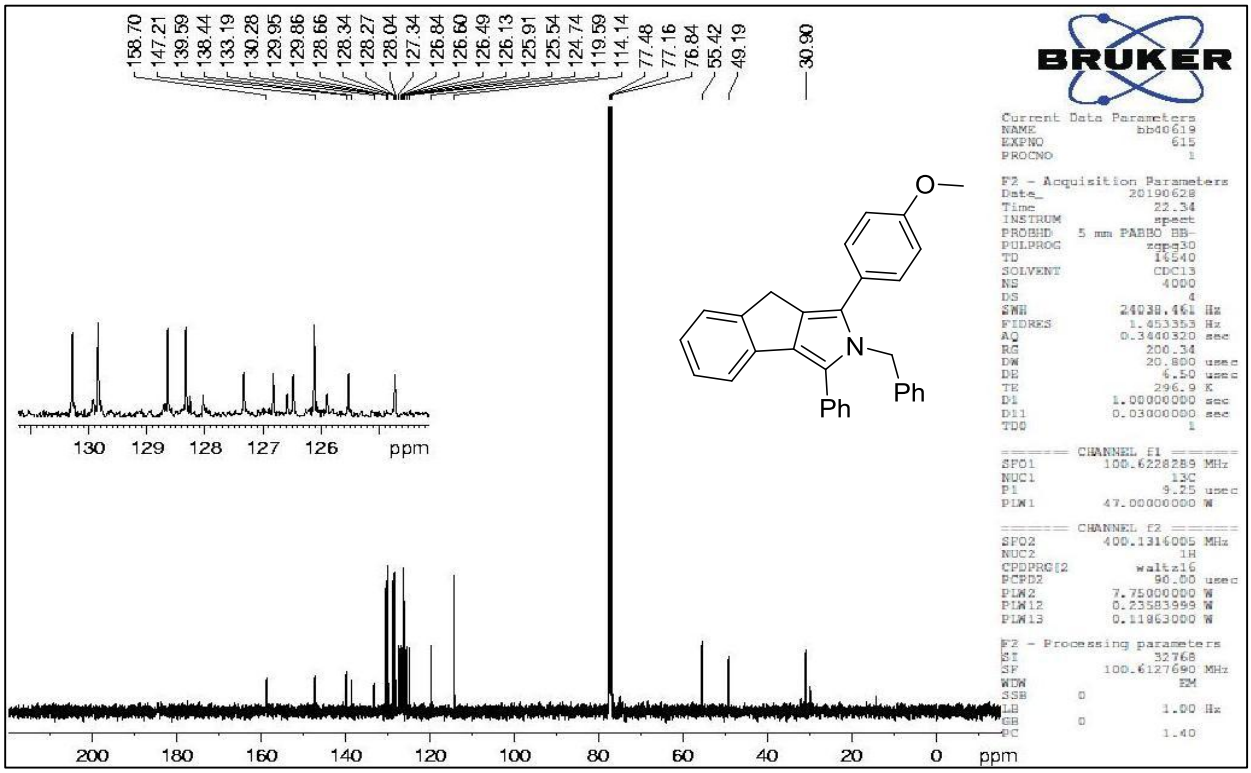

Figure S21. ^{13}C NMR (100 MHz) spectrum of PYROMe1, recorded in $CDCl_3$.

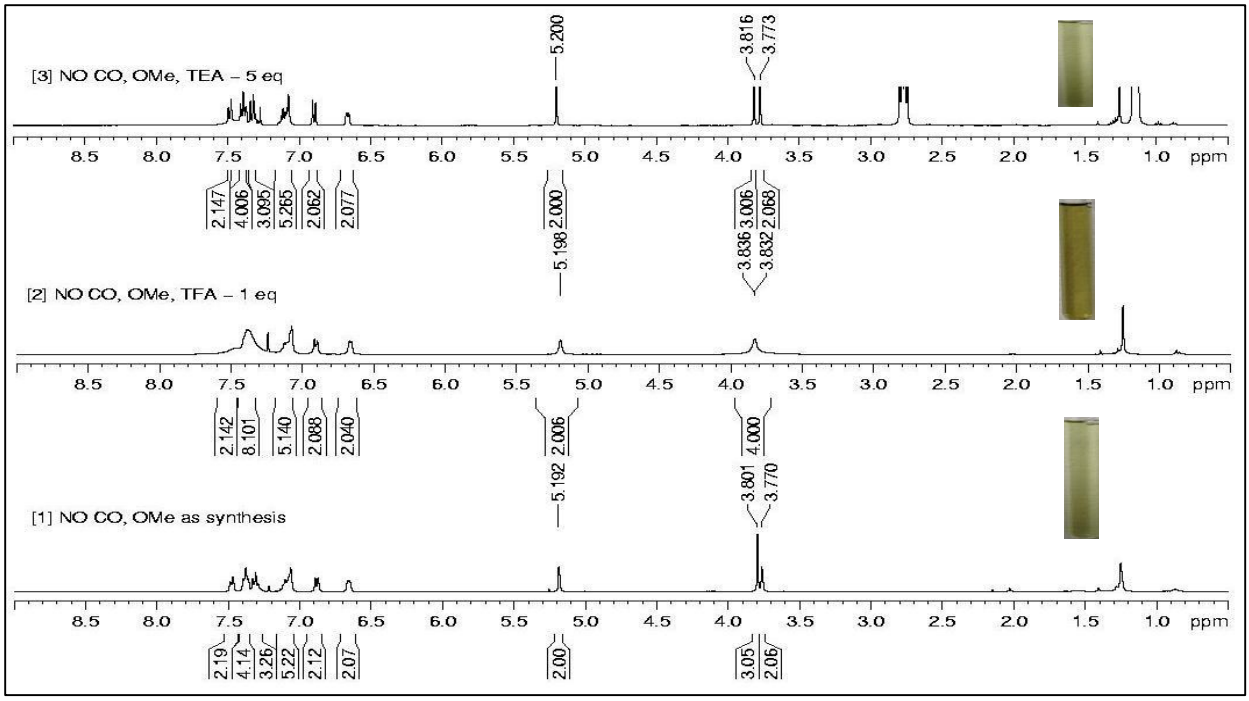

Figure S22. ^{1}H NMR spectra of PYROMe1 in $CDCl_3$ before (bottom) and after (middle) addition of TFA (1 equiv.) followed by excess (5 equiv.) addition of TEA (top). Insets of each spectrum represent respective photographs, taken under normal light.

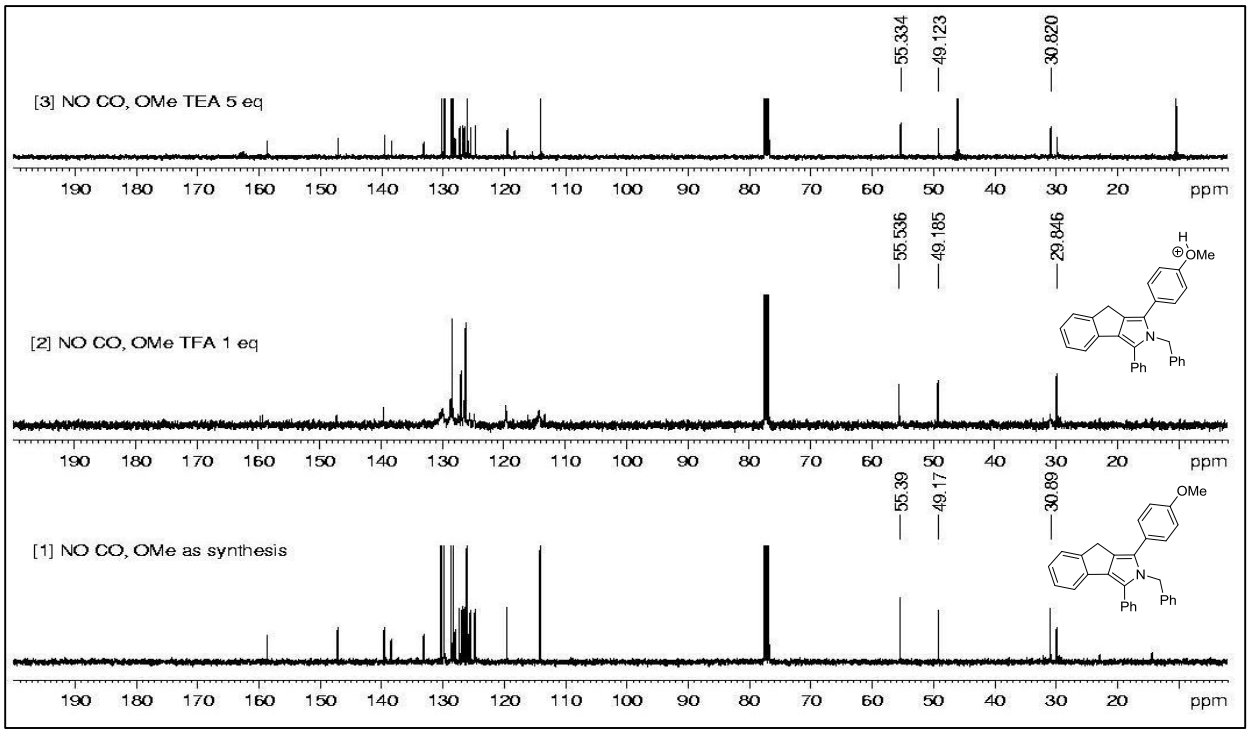

Figure S23. ^{13}C NMR spectra of PYROMe1 in $CDCl_3$ before (bottom) and after (middle) addition of TFA (1 equiv.) followed by excess (5 equiv.) addition of TEA (top).

Synthesis procedure of 2-Benzyl-1,3-diphenyl-2,8-dihydroindeno[1,2-*c*]pyrrole (PYROMe2):

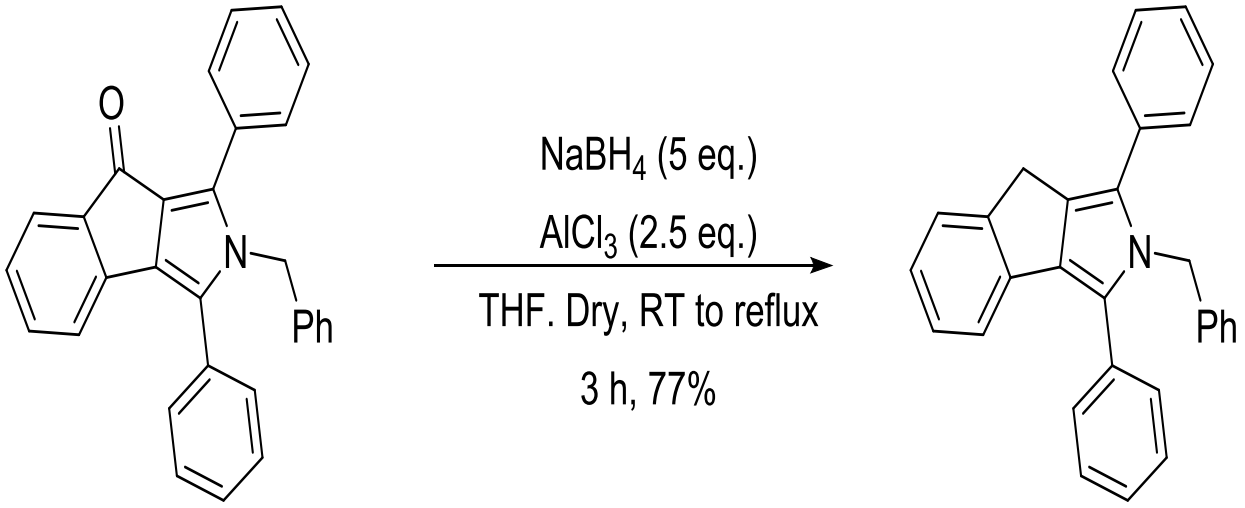

Scheme S3. Represents synthesis procedure of PYROMe2 from the precursor PYR.

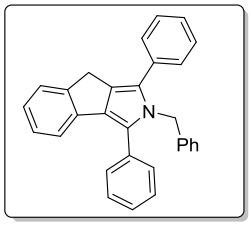

To a solution of PYR (50 mg, 0.12 mmol) in anhydrous THF (5 mL), $NaBH_4$ (22 mg, 0.60 mmol) and $AlCl_3$ (40 mg, 0.30 mmol) were added at RT under nitrogen atmosphere and refluxed for 3 h. Reaction mixture was diluted with water (10 mL), and extracted with ethyl acetate (10 mL). Evaporation of the solvent and purification of the crude reaction mixture by flash chromatography (9:1 hexane: EtOAc) gave the decarbonylated PYROMe2 (37 mg, 0.09 mmol, 77 %) as yellow oil.

^{1}H NMR (400 MHz, $CDCl_3$): δ = 7.50 (2 H, d, *J* = 7.4 Hz), 7.46-7.40 (5 H, m), 7.38 (3 H, d, *J* = 7.8 Hz), 7.36-7.27 (2 H, m), 7.17-7.10 (2 H, m), 7.10-7.05 (3 H, m), 6.69-6.62 (2 H, m), 5.23 (2 H, s) and 3.81 (2 H, s) ppm.

^{13}C NMR (100 MHz, $CDCl_3$): δ = 147.1, 139.4, 138.3, 133.4, 133.0, 130.2, 129.9, 128.8, 128.7, 128.68, 128.63, 128.3, 127.4, 127.2, 126.9, 126.8, 126.5, 126.1, 125.5, 124.8, 119.6, 49.3 and 31.0 ppm.

IR (neat): 3055, 2926, 2858, 1605, 1488, 1246, 1045 and 737 cm^{-1}.

HR ESI-MS: $[C_{30}H_{24}N]^+ = [M+H]^+$ requires 398.1909; found 398.1922.

TLC: R_f = 0.5 (9:1, HXN/EtOAc).

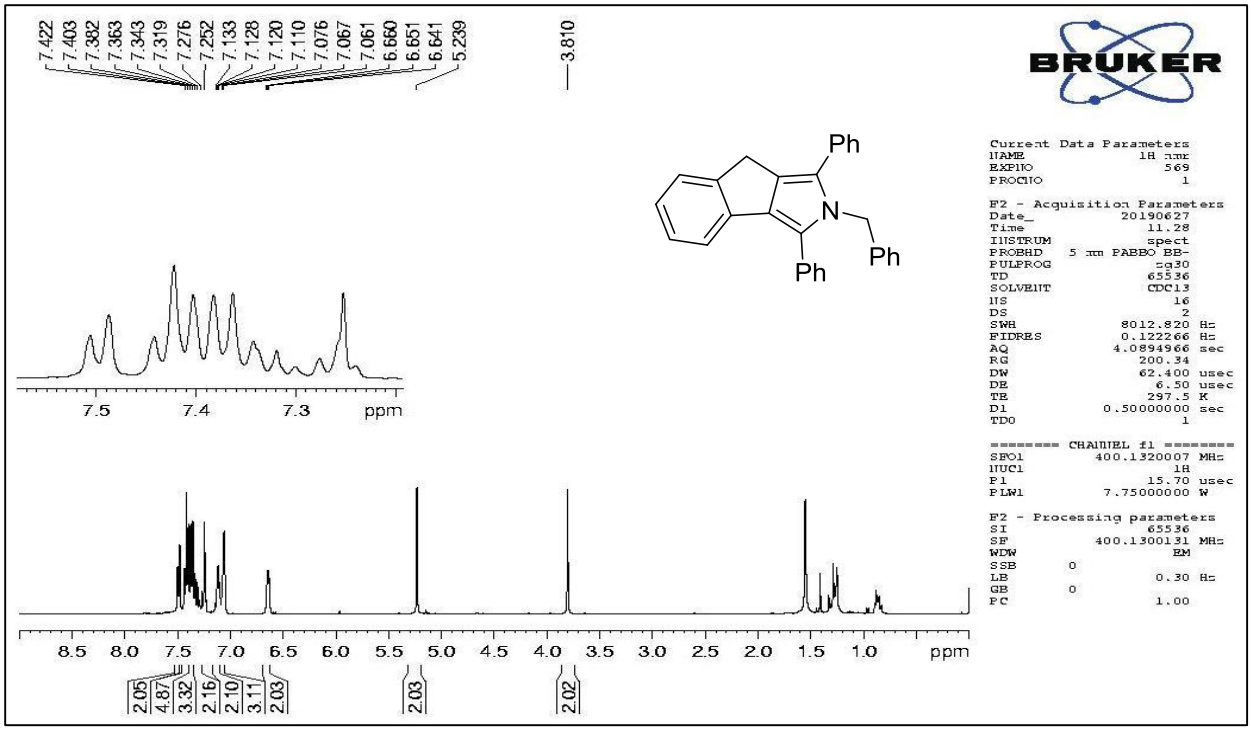

Figure S24. ^{1}H NMR (400 MHz) spectrum of PYROMe2, recorded in $CDCl_3$.

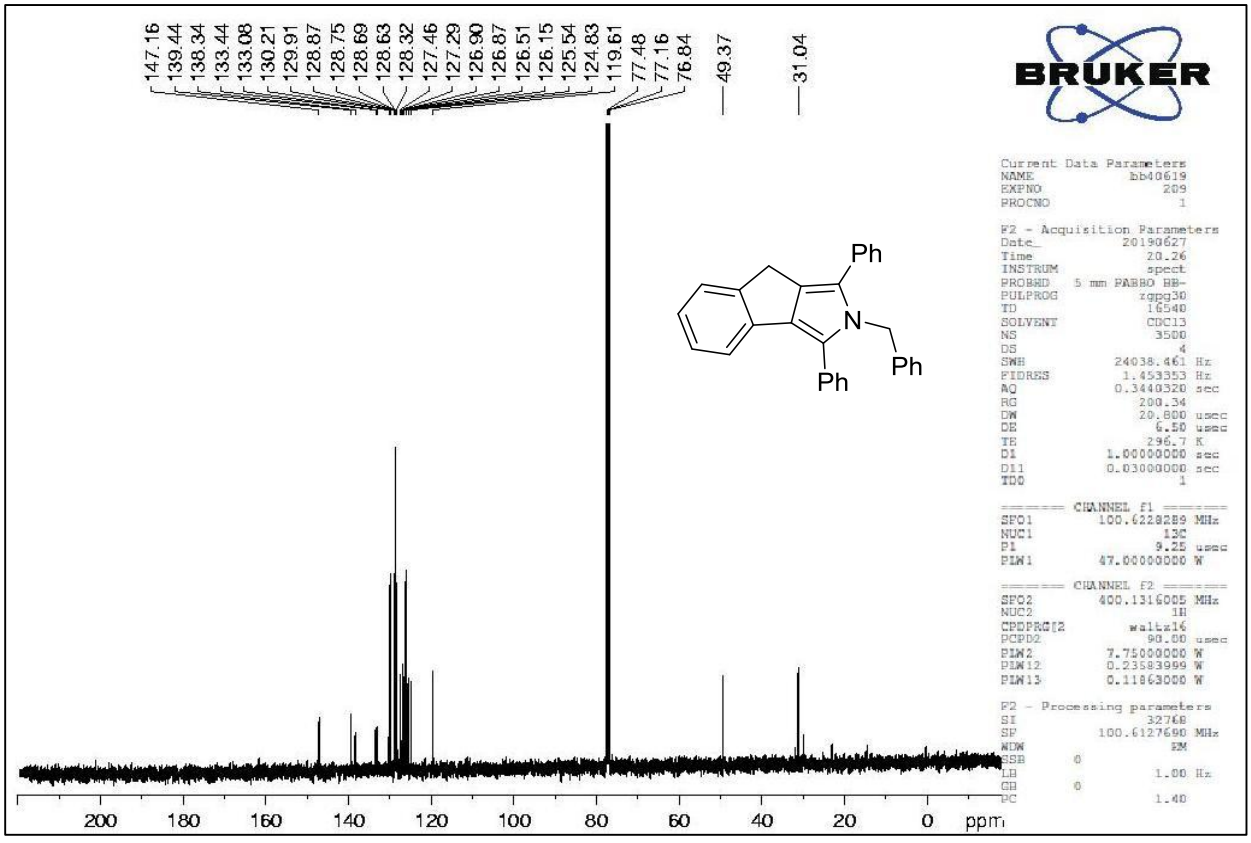

Figure S25. ^{13}C NMR (100 MHz) spectrum of PYROMe2, recorded in $CDCl_3$.

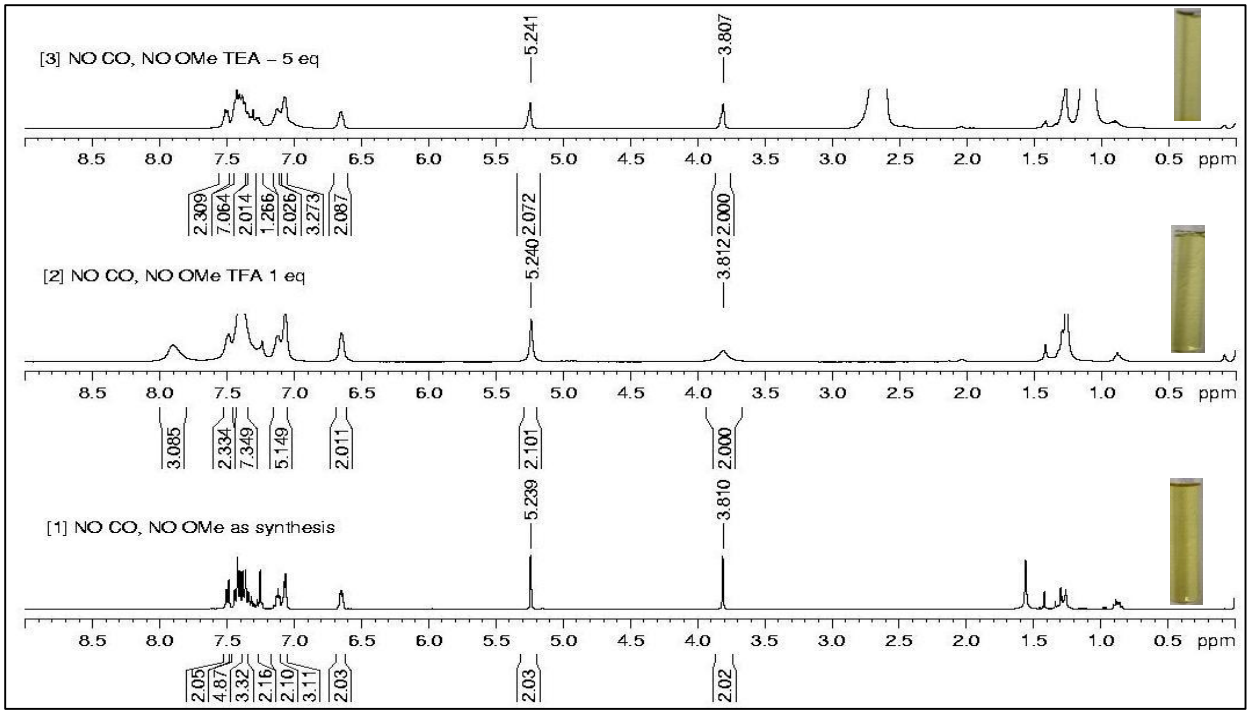

Figure S26. ^{1}H NMR spectra of PYROMe2 in $CDCl_3$ before (bottom) and after (middle) addition of TFA (1 equiv.) followed by excess (5 equiv.) addition of TEA (top). Insets of each spectrum represent respective photographs, taken under normal light.

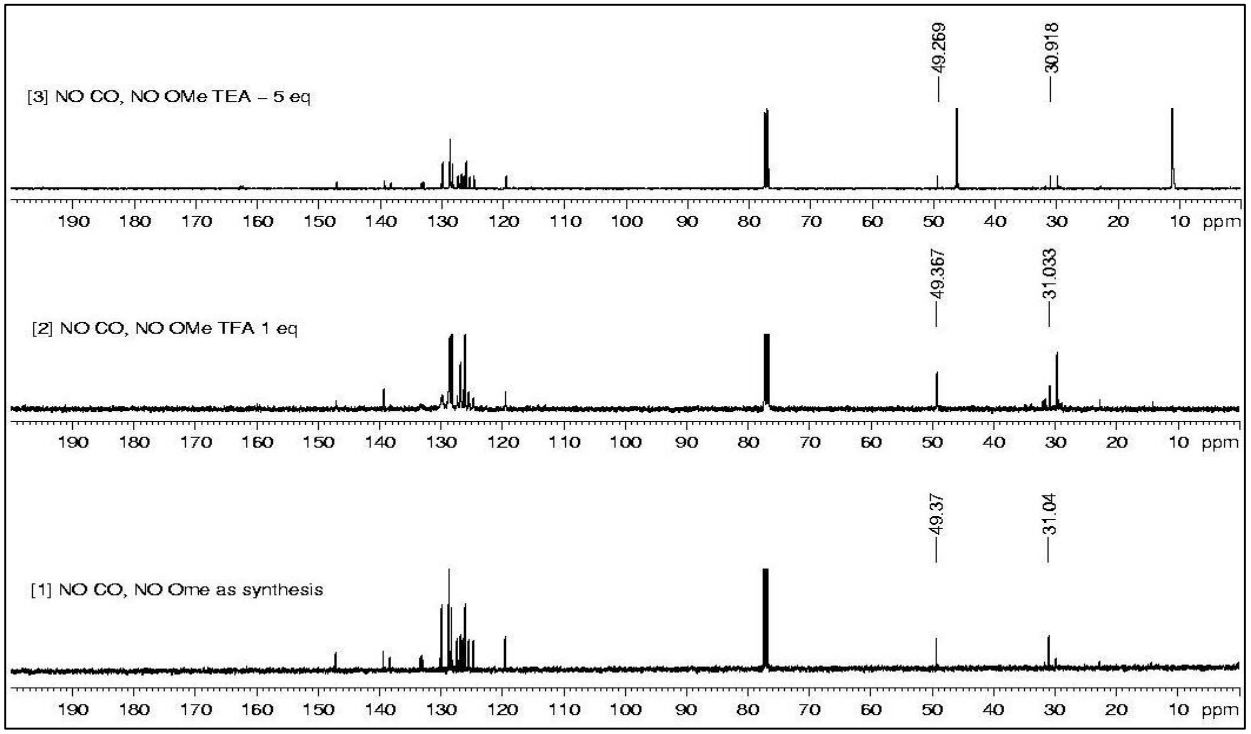

Figure S27. ^{13}C NMR spectra of PYROMe2 in $CDCl_3$ before (bottom) and after (middle) addition of TFA (1 equiv.) followed by excess (5 equiv.) addition of TEA (top).

The Stern-Volmer equation (eq. S5) and the Hill equation (eq. S6), utilized for determination of quenching (K_{SV}) and binding constants (B) along with binding number (n) between analyte and probe are given below:

$$\frac{I_0}{I} = 1 + K_{SV}[Q] \qquad (S5)$$

where, I_0 and I are the fluorescence intensity of probe (PYROMe) in absence and presence of analyte (TFA), K_{SV} is the Stern-Volmer constant, and [Q] is the analyte concentration.

$$\log\left[\frac{(I - I_{min})}{(I_{max} - I)}\right] = nlog[Q] + B \qquad (S6)$$

where, I_{min} and I_{max} and are the minimum and maximum fluorescence intensities of probe in presence and absence of the saturated analyte, I is the fluorescence intensity of probe in presence of certain amount of analyte, n is the number of analyte molecules bounded per probe molecule, [Q] is the quencher concentration and B is the binding constant between analyte and probe.

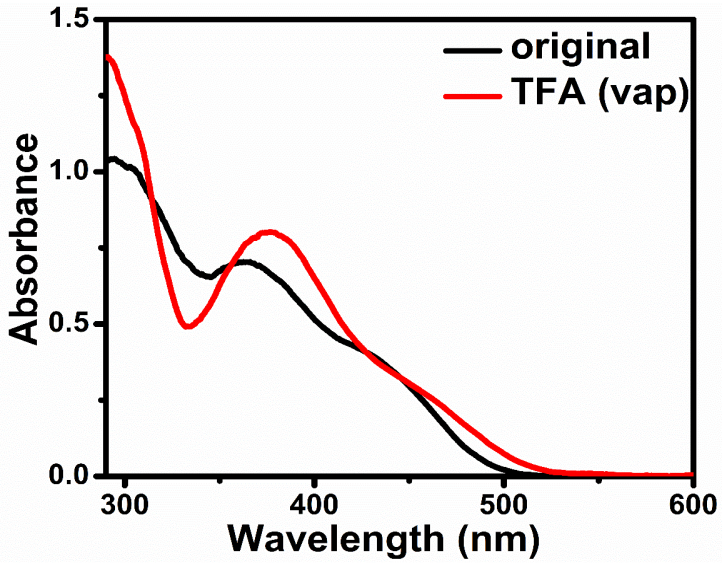

Figure S28. Absorption spectra of PYROMe thin film before (black) and after (red line) treatment with saturated TFA vapor for 60 seconds.

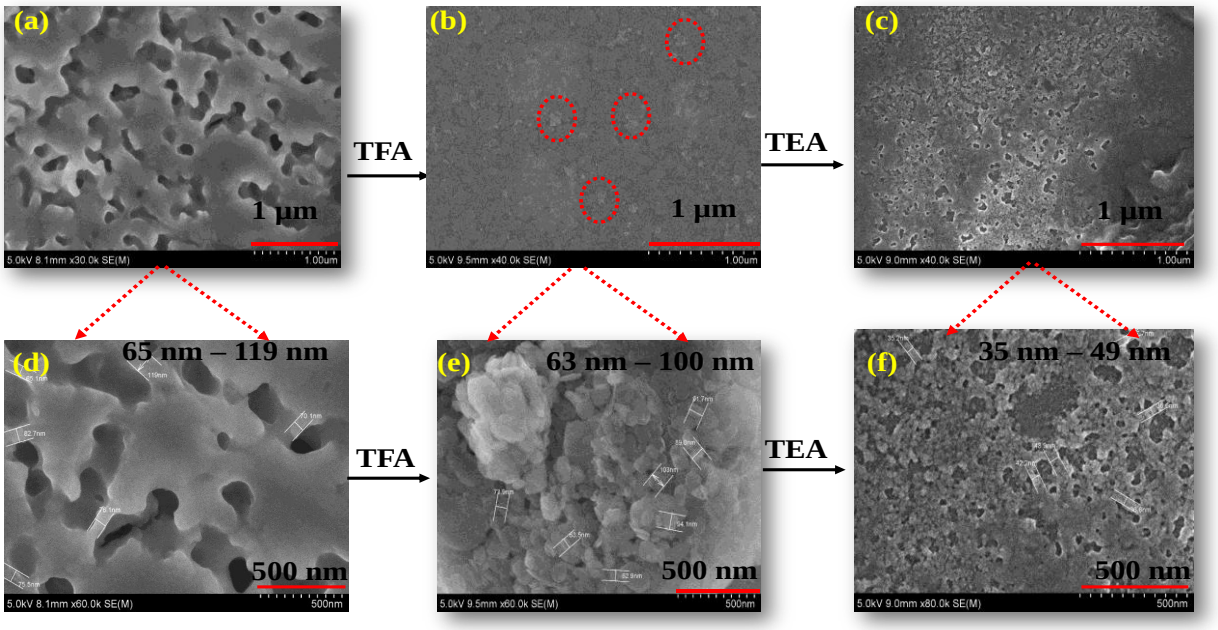

Figure S29. SEM images of the developed film of PYROMe on ITO substrate, recorded (a, d) before and (b, e) after treatment with saturated TFA vapor and subsequently (c, f) with saturated TEA vapor.

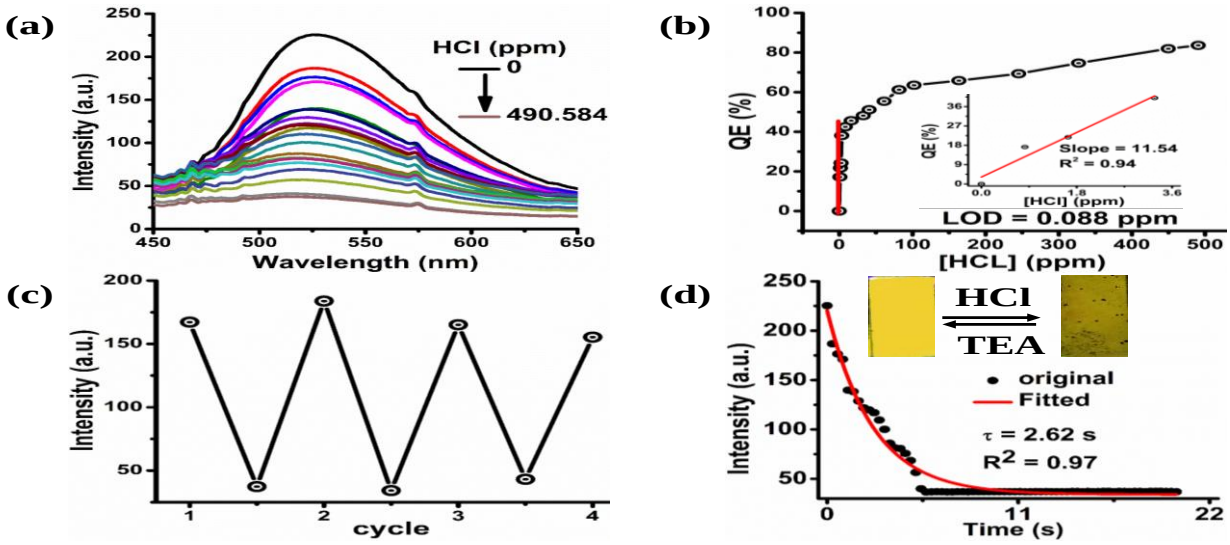

Figure S30. (a) Variation in fluorescence emission spectra (λ_{ex} = 350 nm) of PYROMe thin film at 527 nm with increased HCl vapor. (b) Plot of concentration dependent fluorescence quenching efficiency [QE (%)] under increased HCl vapor concentration. Corresponding inset represents linear variation of QE (%) under low vapor concentration (< 3.27 ppm). (c) Reversible fluorescence 'on-off' switching by alternate exposure of the thin to saturated HCl (10 minute) and saturated TEA vapors (20 minutes) respectively. (d) Time-course of intensity quenching of the thin film upon exposure to saturated HCl vapor. Corresponding inset represents change in fluorescence color of the thin film upon exposure to saturated acid and base vapors alternatively.

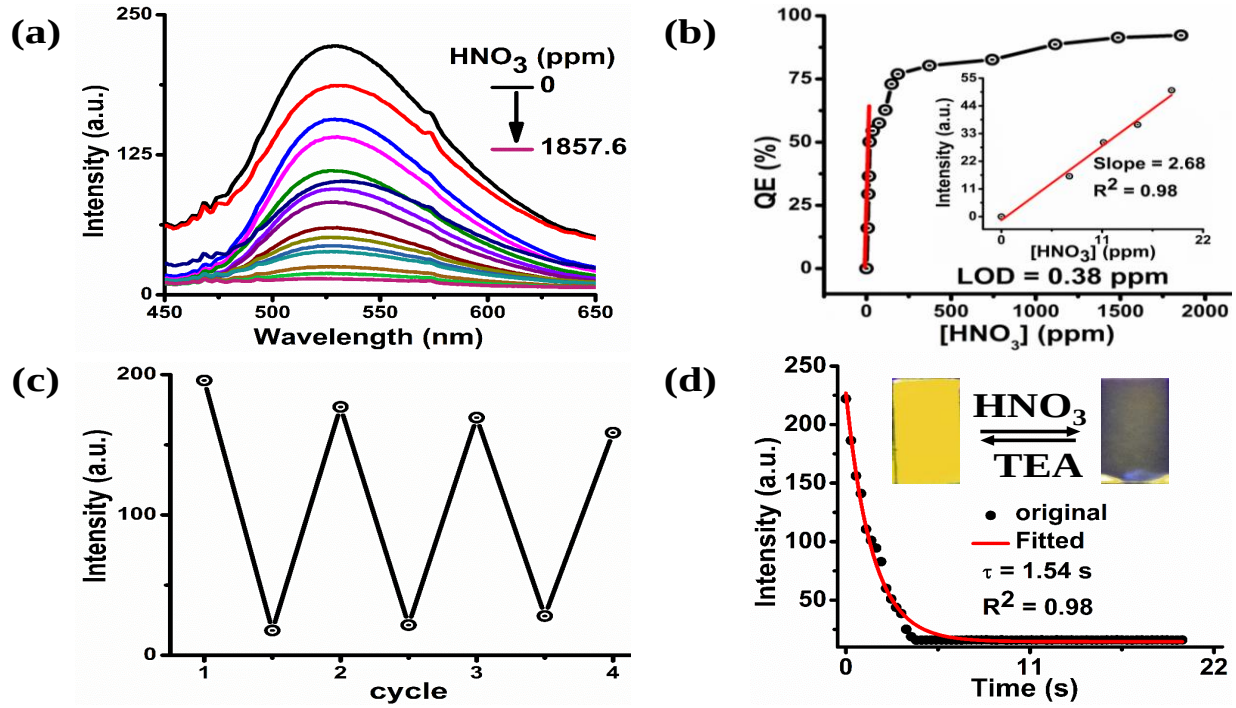

Figure S31. (a) Variation in fluorescence emission spectra (λ_{ex} = 350 nm) of PYROMe thin film at 527 nm with increased HNO_3 vapor. (b) Plot of concentration dependent fluorescence quenching efficiency [QE (%)] under increased HNO_3 vapor concentration. Corresponding inset represents linear variation of QE (%) under low vapor concentration (<37.15 ppm). (c) Reversible fluorescence 'on-off' switching by alternate exposure of the thin to saturated HNO_3 (2 minutes) and saturated TEA vapors (20 minutes) respectively. (d) Time-course of intensity quenching of the thin film upon exposure to saturated HNO_3 vapor. Corresponding inset represents change in fluorescence color of the thin film upon exposure to saturated acid and base vapors alternatively.

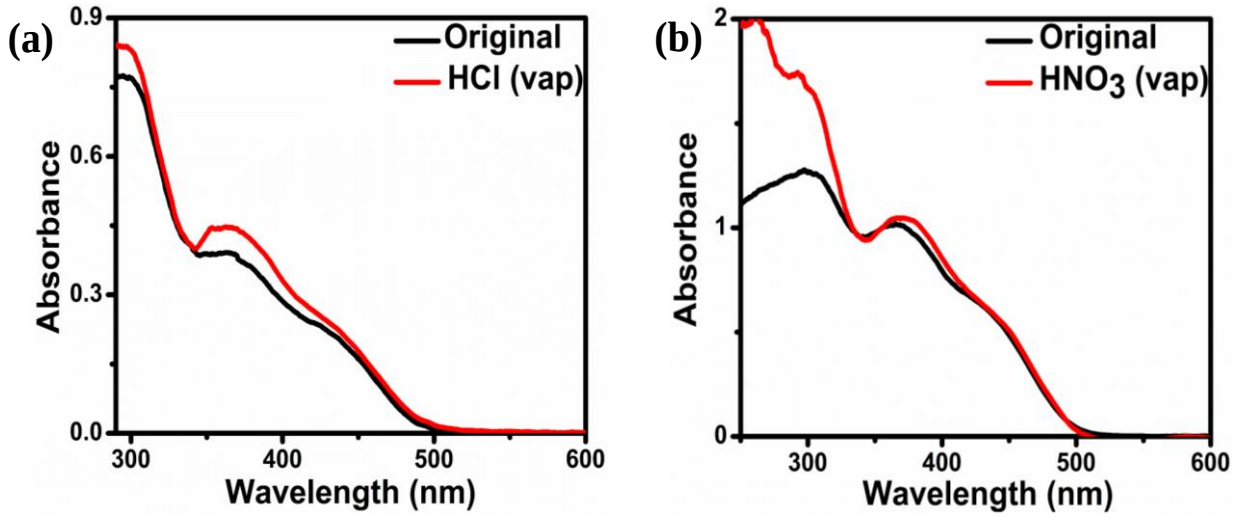

Figure S32. Absorption spectra of PYROMe thin film before (black) and after (red line) treatment with (a) saturated HCl vapor and (b) HNO_3 vapor for 10 minutes and 2 minutes respectively.

Detection of TFA from water based on paper strip study:

For this, the self-assembled portable strips of PYROMe were fabricated on whatman filter paper based on a reported procedure.[8] Subsequently, those strips were treated with different concentration of aqueous TFA solutions and the evolved quenched spots were monitored under UV light (λ_{ex} = 365 nm).

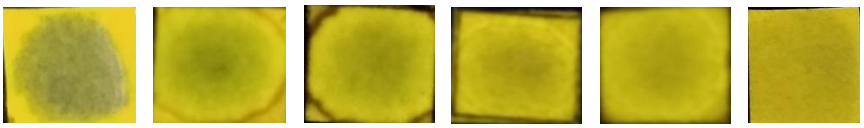

10^{-1} M 10^{-2} M 10^{-3} M 10^{-4} M 10^{-5} M 10^{-6} M

Figure S33. Paper strips of PYROMe showing the fluorescence quenching over the spotted area after addition of different concentrations of aqueous TFA, monitored under UV light (λ_{ex} = 365 nm).

From Figure S33, it can be observed that the fabricated strips were capable to detect TFA from water until the limit of 1×10^{-6} M. Based on the above observation, detection limit (DL) of PYROMe strips towards aqueous TFA was calculated to be as low as 3.42 ng/cm^2, by adding 30 µL of 1×10^{-6} M aqueous TFA solution on the strip, covering 1cm^2 area.

The quantitative analysis of DL is as follows:

$$DL = [10^{-6}\ \text{mol/L} \times 114.02\ \text{g/mol} \times 30\times10^{-6}\ \text{L}]/\text{cm}^2$$

$$= 342.06\times10^{-11}\ \text{g/cm}^2$$

$$= 3.42\times10^{-9}\ \text{g/cm}^2$$

$$= 3.42\ \text{ng/cm}^2;$$ where molecular weight of TFA = 114.02 g/mol.

From the above result it can be inferred that the fabricated strip of PYROMe can detect TFA at reasonably low concentrations from water which might open up an efficient tool for detection of hazardous species from water.

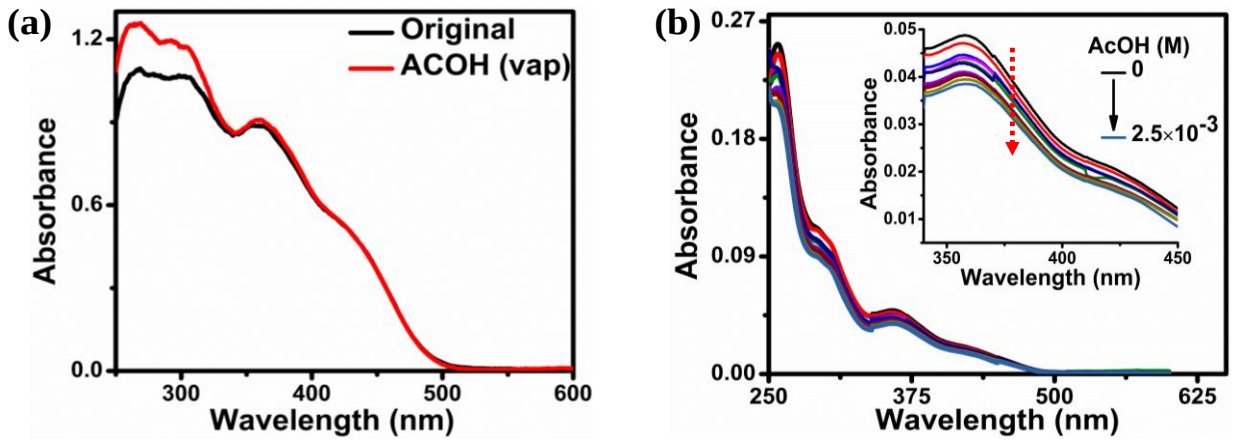

Figure S34. (a) Absorption spectra of PYROMe thin film before (black) and after (red line) treatment with saturated AcOH vapor. (b) Absorption spectra of PYROMe in DCM (concentration = 10 µM) with increasing addition of AcOH represents almost unaltered spectral behavior without generation of any new red-shifted absorption peak rather a gradual decreament (Inset of Figure S34b) even in presence of excess amount of AcOH.

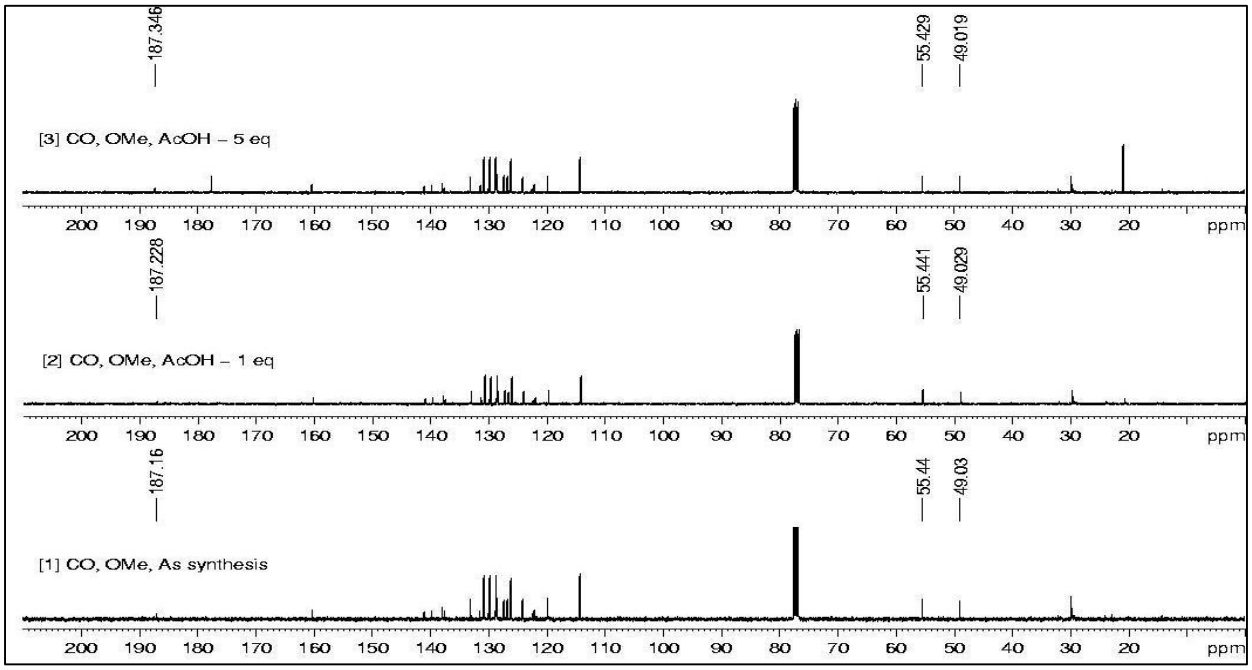

Figure S35: ^{13}C NMR spectra of PYROMe in $CDCl_3$ before (bottom) and after addition of 1 equiv. (middle) and excess (5 equiv.) amount of AcOH (top).

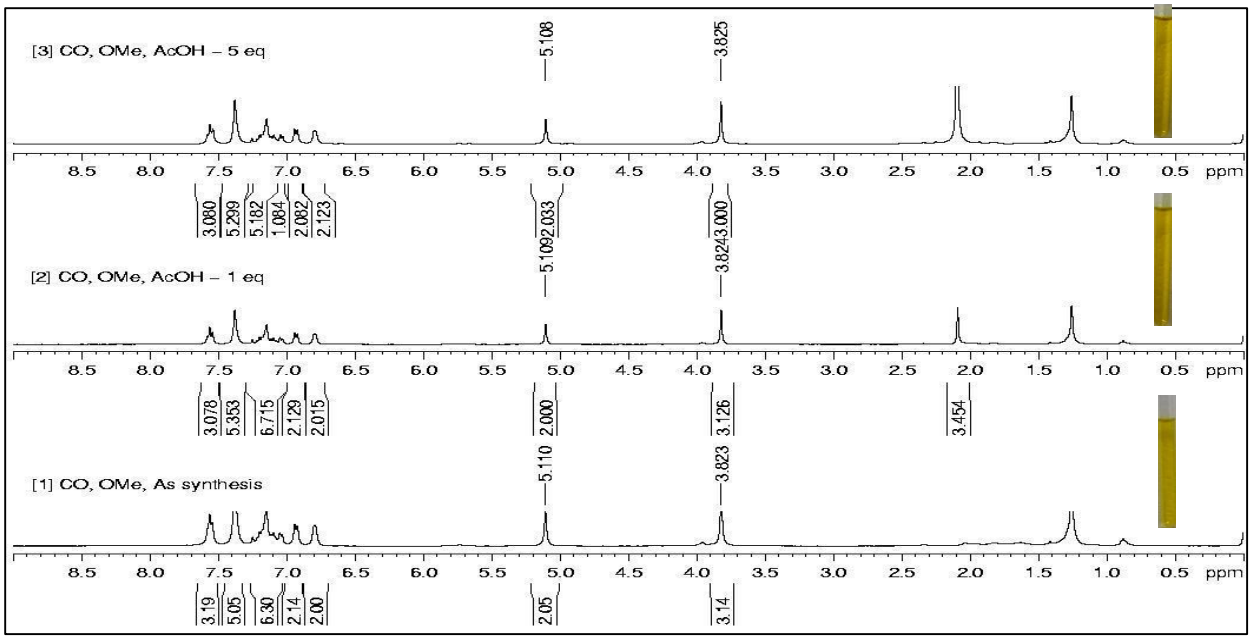

Figure S36. ^{1}H NMR spectra of PYROMe in $CDCl_3$ before (bottom) and after addition of 1 equiv. (middle) and excess (5 equiv.) amount of AcOH (top). Insets represent the respective photographs under normal light.

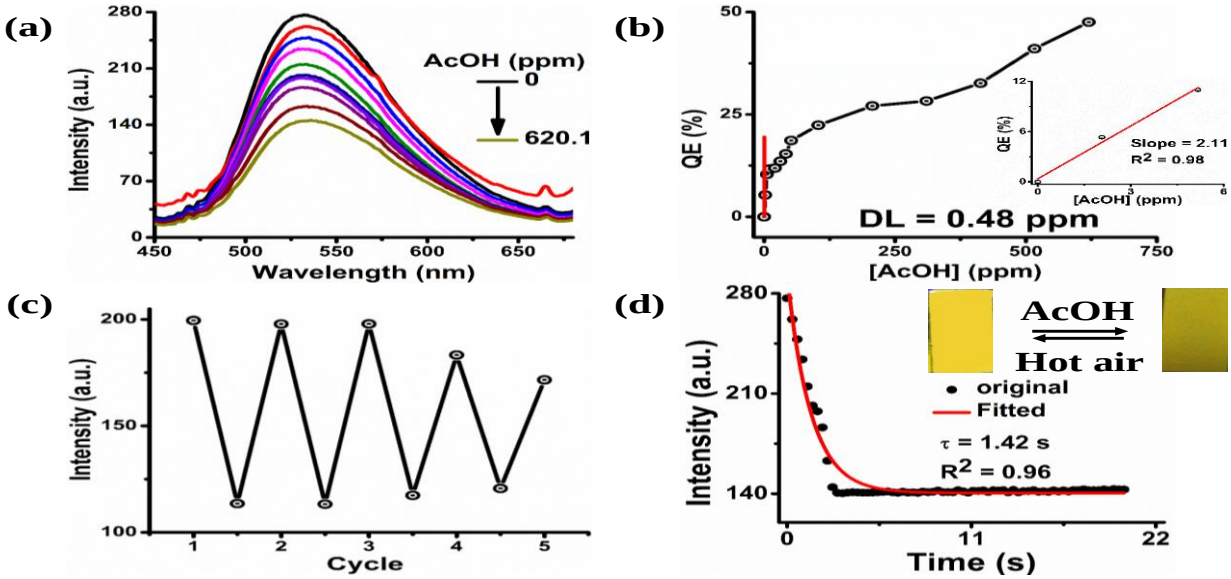

Figure S37. (a) Variation in fluorescence emission spectra (λ_{ex} = 350 nm) of PYROMe thin film at 527 nm with increased AcOH vapor. (b) Plot of concentration dependent fluorescence quenching efficiency [QE (%)] under increased AcOH vapor concentration. Corresponding inset represents linear variation of QE (%) under low vapor concentration (<10.33 ppm). (c) Reversible fluorescence 'on-off' switching by alternate exposure of the thin to saturated AcOH (2 minutes) and hot air (20 minutes) respectively. (d) Time-course of intensity quenching of the thin film upon exposure to saturated AcOH vapor. Corresponding inset represents change in fluorescence color of the thin film upon exposure to saturated acid and hot air alternatively.

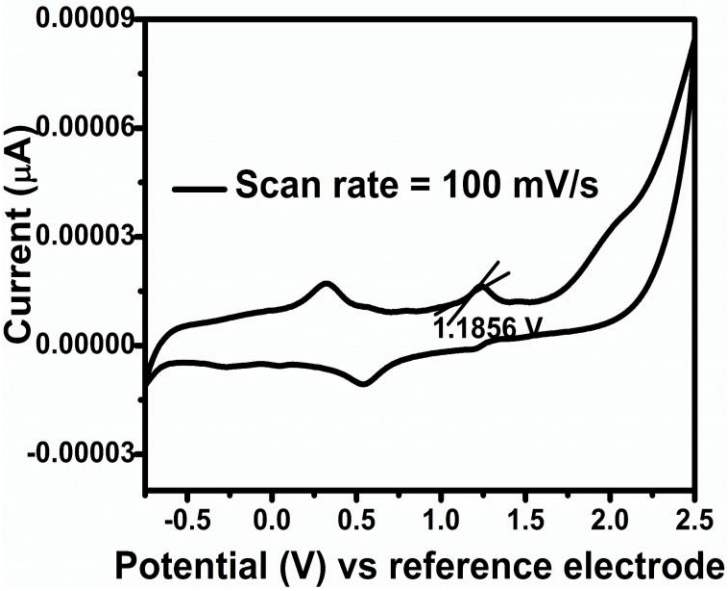

Figure S38. Cyclic voltammogram of PYROMe in ACN at 100 mV/s scan rate (concentration = 1 mM) represents onset oxidation potential of 1.1856 V.

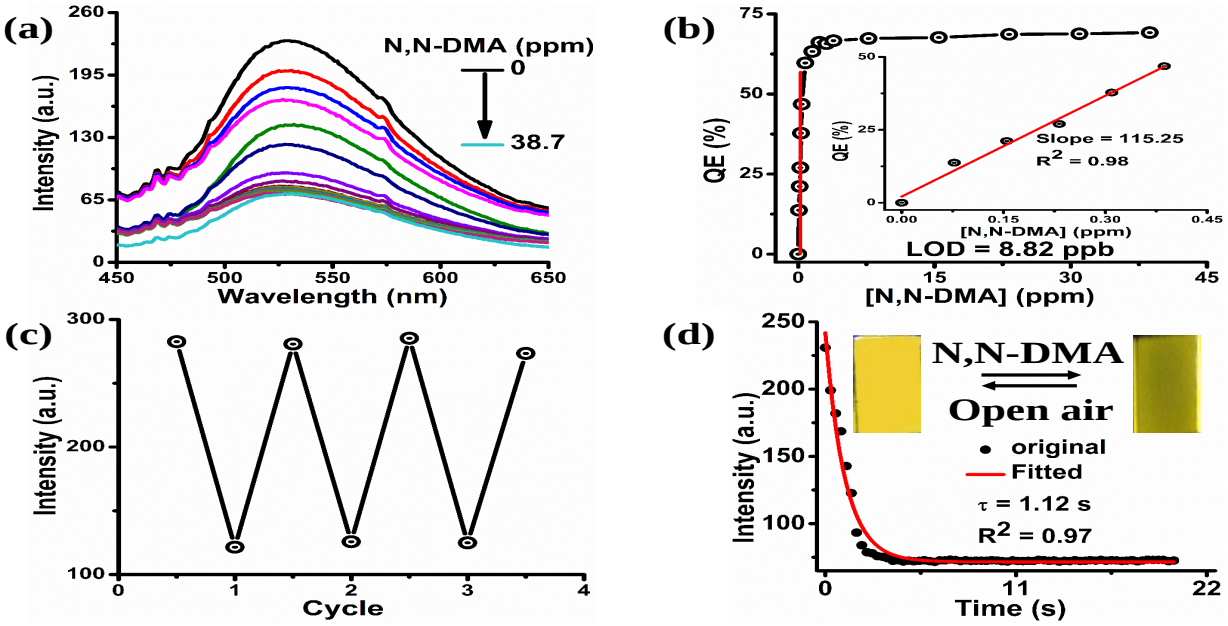

Figure S39. (a) Variation in fluorescence emission spectra (λ_{ex} = 350 nm) of PYROMe thin film at 527 nm with increased *N*,*N*-dimethylaniline vapor. (b) Plot of concentration dependent fluorescence quenching efficiency [QE (%)] under increased *N*,*N*-dimethylaniline vapor concentration. Corresponding inset represents linear variation of QE (%) under low vapor concentration (< 0.77 ppm). (c) Reversible fluorescence 'on-off' switching by alternate exposure of the thin to saturated *N*,*N*-dimethylaniline (5 minutes) and open air (30 minutes) respectively. (d) Time-course of intensity quenching of the thin film upon exposure to saturated *N*,*N*-dimethylaniline vapor. Corresponding inset represents change in fluorescence color of the thin film upon exposure to saturated amine and open air alternatively.

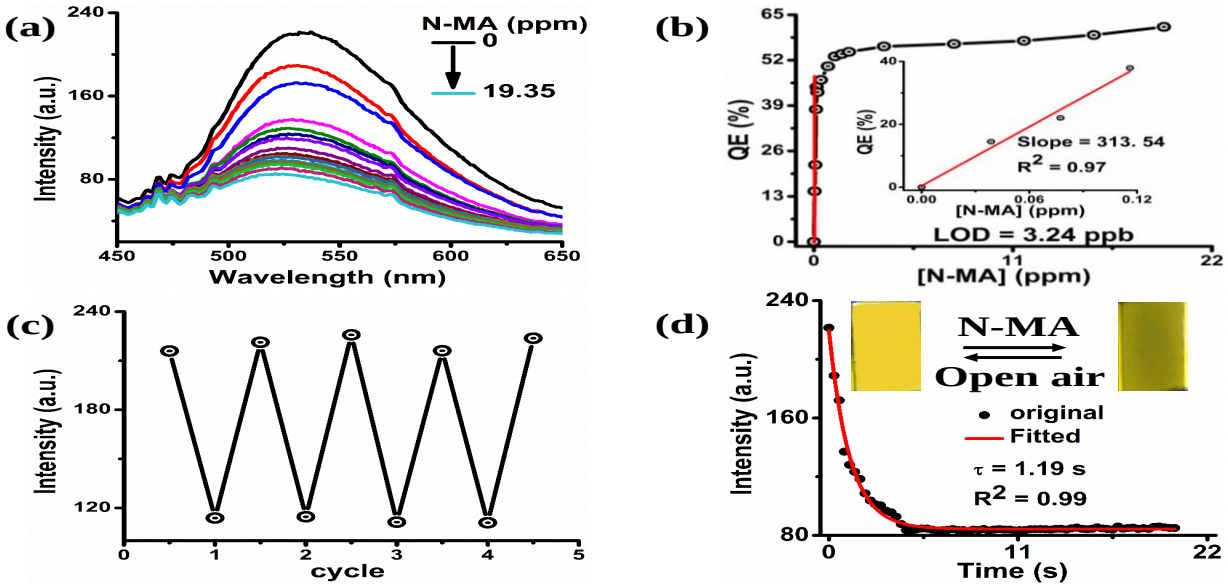

Figure S40. (a) Variation in fluorescence emission spectra (λ_{ex} = 350 nm) of PYROMe thin film at 527 nm with increased *N*-methylaniline vapor. (b) Plot of concentration dependent fluorescence quenching efficiency [QE (%)] under increased *N*-methylaniline vapor concentration. Corresponding inset represents linear variation of QE (%) under low vapor concentration (< 0.11ppm). (c) Reversible fluorescence 'on-off' switching by alternate exposure of the thin to saturated *N*-methylaniline (5 minutes) and open air (30 minutes) respectively. (d) Time-course of intensity quenching of the thin film upon exposure to saturated *N*-methylaniline vapor. Corresponding inset represents change in fluorescence color of the thin film upon exposure to saturated amine and open air alternatively.

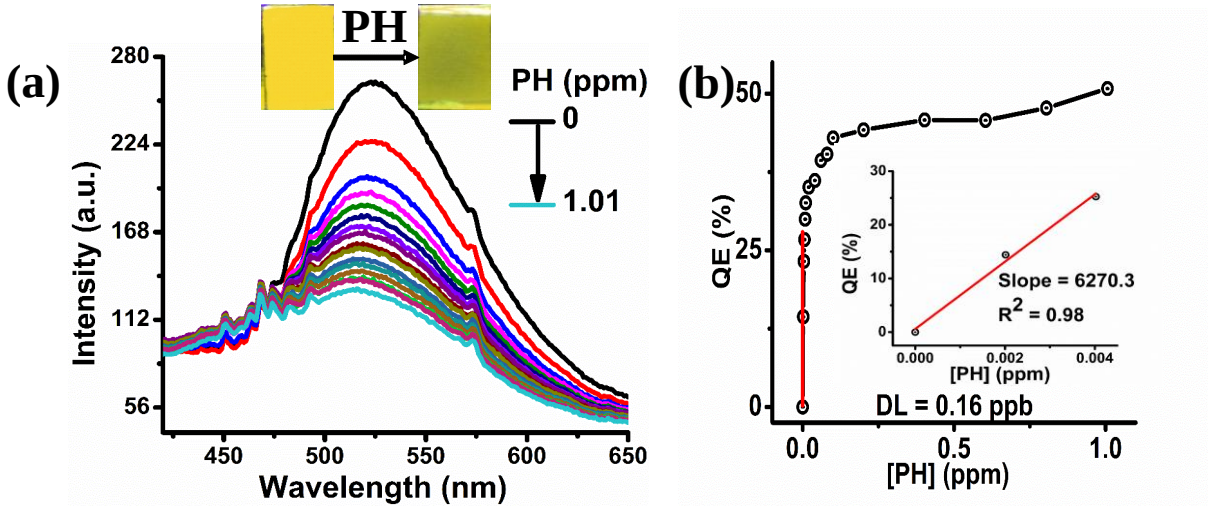

Figure S41. (a) Variation in fluorescence emission spectra (λ_{ex} = 350 nm) of PYROMe thin film at 527 nm with increased addition of phenylhydrazine vapor. (b) Plot of concentration dependent fluorescence quenching efficiency [QE (%)] under increased phenylhydrazine vapor concentration. Corresponding inset represents linear variation of QE (%) under low vapor concentration (< 0.006 ppm).

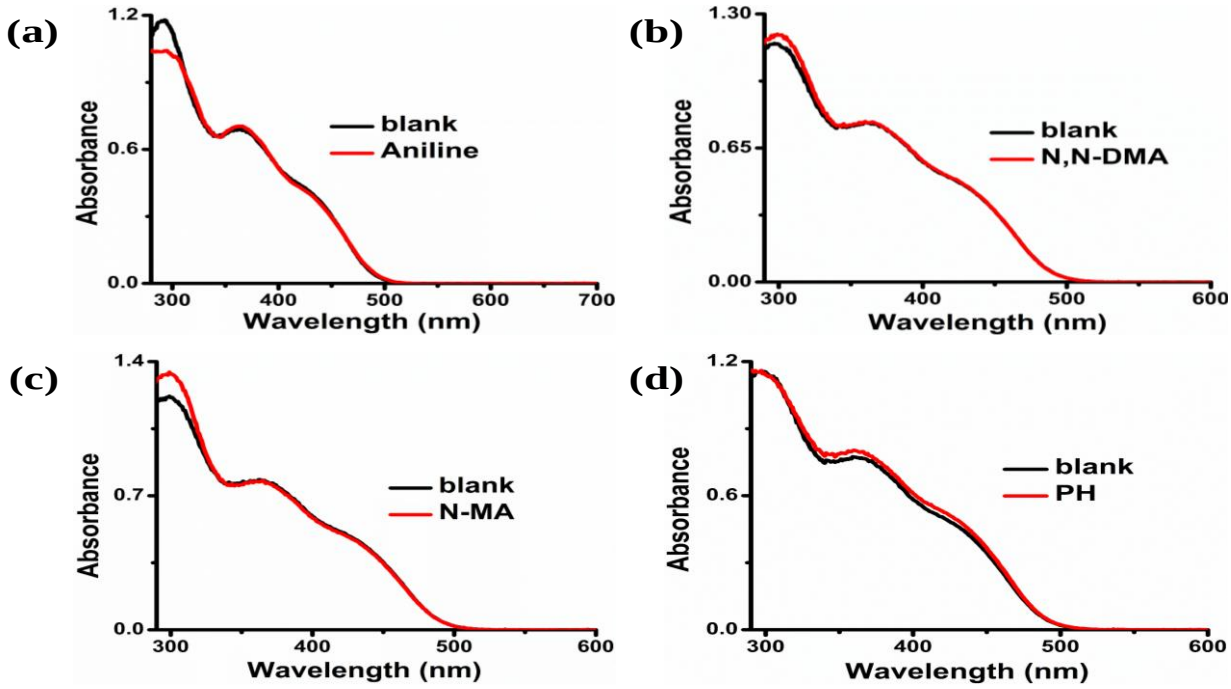

Figure S42. UV-visible absorption spectra of PYROMe thin film in presence of saturated (a) aniline, (b) *N*,*N*-Dimethylaniline, (c) *N*-methylaniline and (d) phenylhydrazine vapors.

Detection of aniline from water based on paper strip study:

Similar to the above observation, detection of aniline from water was performed by treating the fabricated paper strips with different concentrations of aqueous aniline followed by monitoring the quenched spots under UV light. From Figure S43 it can be inferred that, the fabricated strips can detect aniline until the limit of 1×10^{-5} M and the DL was found to be as low as 27.94 ng/cm^2.

10^{-1} M **10^{-2} M** **10^{-3} M** **10^{-4} M** **10^{-5} M**

Figure S43. Paper strips of PYROMe showing the fluorescence quenching over the spotted area after addition of different concentrations of aqueous aniline, monitored under UV light (λ_{ex} = 365 nm).

The quantitative analysis for DL is shown here:

$$DL = [10^{-5}\ mol/L \times 93.13\ g/mol \times 30\times10^{-6}\ L]/cm^2$$

$$= 2.7939\times10^{-8}\ g/cm^2$$

$$= 27.94\times10^{-9}\ g/cm^2$$

$= 27.94\ ng/cm^2$; where molecular weight of aniline = 93.13 g/mol and the volume of the added aniline solution = 30 µL.

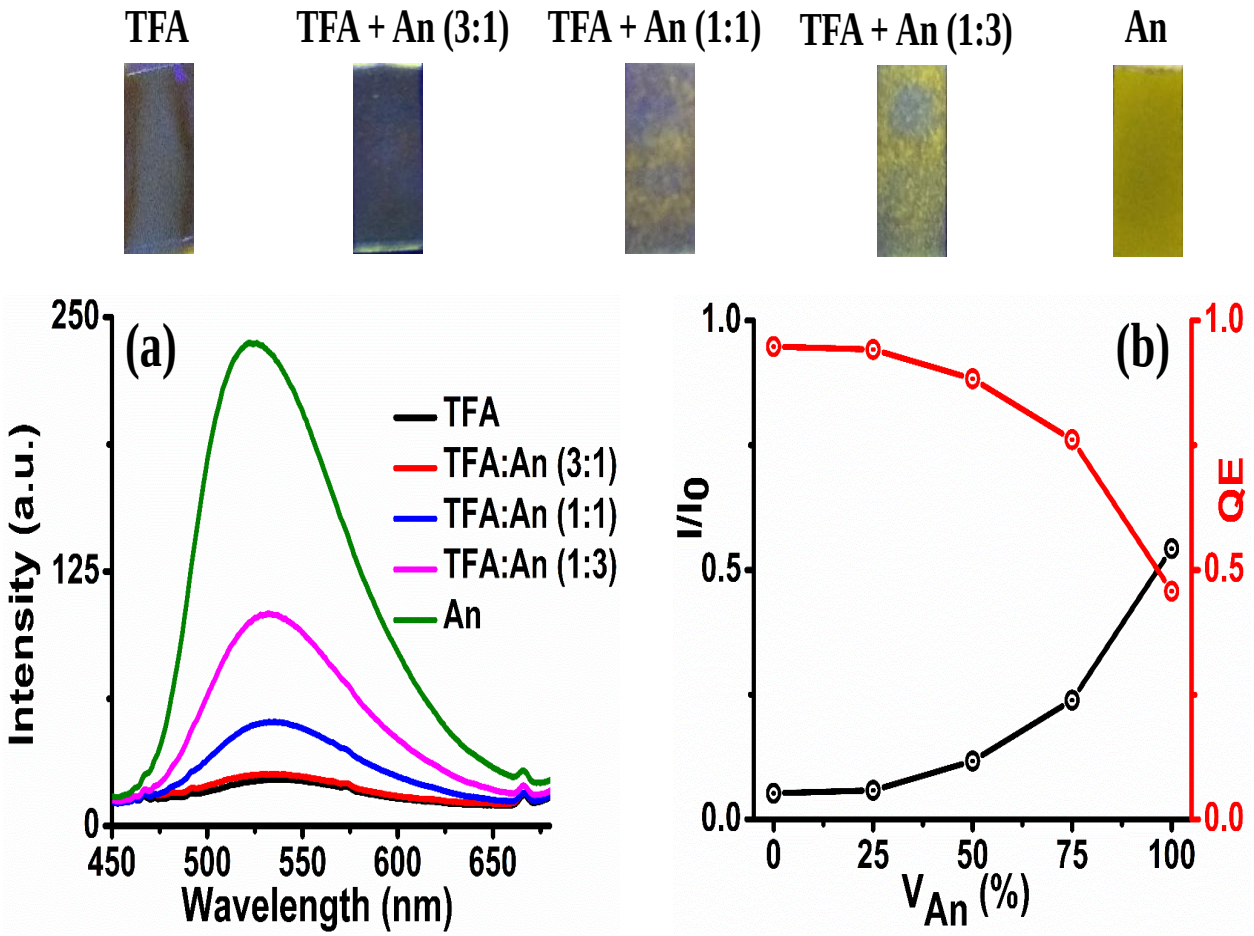

Figure S44. (a) Emission spectra of PYROMe thin film recorded after exposure to the saturated vapors of TFA (black), TFA + Aniline (An) [3:1] (red), TFA + An [1:1] (blue), TFA + An [1:3] (pink), and only Aniline (green) for 2 minutes (λ_{ex} = 350 nm). (b) Variation in I/I_0 (black) and QEs (red) of PYROMe thin film with respect to the increased volume fraction of aniline in TFA. Top of figures (a) and (b) represents the photographs of the film taken under UV light after exposure to TFA, aniline and their different mixtures for 2 minutes.

Table S10. Quenching efficiency [QE (%)] of PYROMe thin film in presence of examined saturated solvent vapors

Common organic solvent vapors	
Analytes	QE (%)
Acetone	2.97
Ethyl acetate	2.45
Tetrahydrofuran	3.41
Chloroform	5.31
Dichloromethane	0.57
Hexane	4.56
Ethanol	4.24
Diethyl ether	3.35
Toluene	0.27
water	-1.52

Table S11. Quenching efficiency of PYROMe thin film in presence of saturated amine (both aromatic and aliphatic) vapors along with free energy change (ΔG) associated with PET from analytes to probe

Amine vapors		
Analytes	QE (%)	Driving force [ΔG (-eV)][a]
Aniline	57.54	2.59
N,*N*-Dimethylaniline	69.18	2.51
N-Methylaniline	61.53	2.59
Phenylhydrazine	50.81	3.31
Dibutylamine	-1.82	1.98
n-butylamine	-0.84	1.66
Tripropylamine	-4.33	-
Cyclohexylamine	-2.36	-
Triethylamine	0.52	2.06
Diisopropylamine	-1.25	-
Ammonia	-4.23	-

[a]The driving force for PET from amines to PYROMe was realized via change in free energy (ΔG) associated with the process, which was calculated using the Rehm-Waller equation[9]: $\Delta G = e\left[E^0_{\left(\frac{D}{D^+}\right)} - E^0_{\left(\frac{A}{A^-}\right)}\right] - \Delta E_{00}$, where $E^0_{\left(\frac{D}{D^+}\right)}$ and $E^0_{\left(\frac{A}{A^-}\right)}$ represent oxidation and reduction potentials of electron donor and acceptor respectively, and ΔE_{00} is the singlet excitation energy.

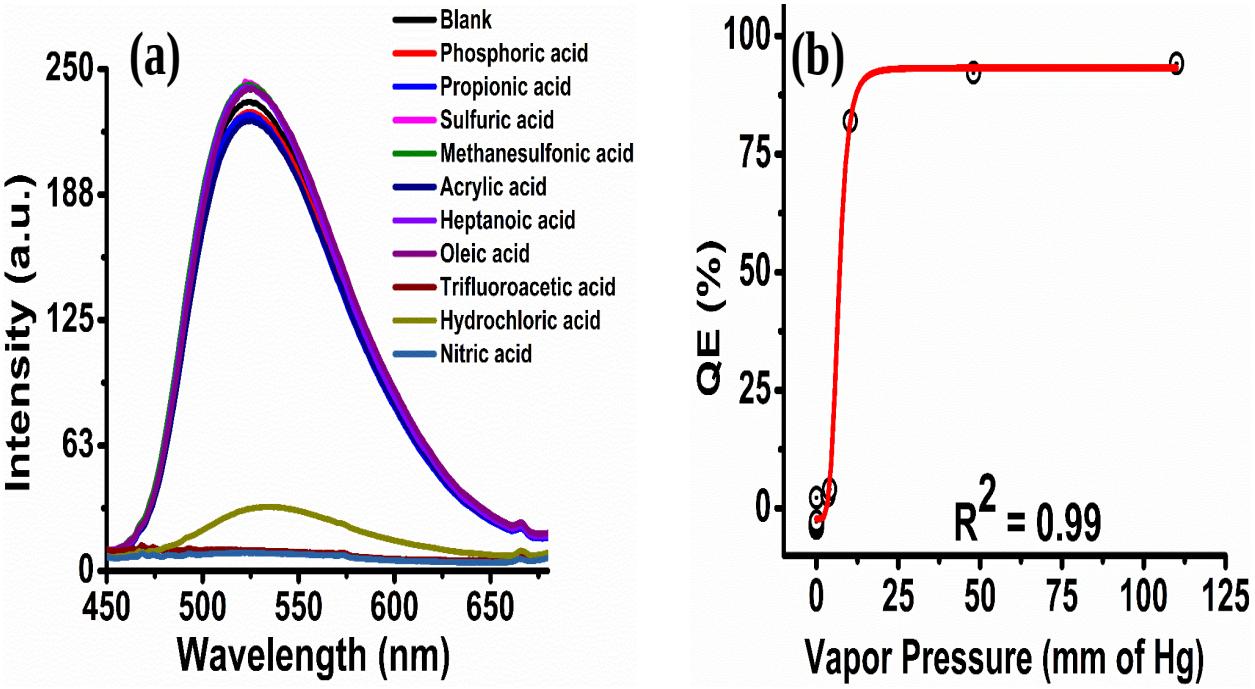

Figure S45. (a) Emission intensity of PYROMe thin film recorded after exposure to the vapors of different tested acids for 5 minutes. (b) Variation of QE (%)s with respect to the vapor pressures of different acids.

Table S12. Comparison table of PYROMe showing dual sensory response for volatile acid and aromatic amines with previously reported literatures

Sr. no	Publication	compound	Properties studied	Dual sensory response	
				Acid vapor	Aromatic amine vapor
1	*J. Mater. Chem. C* **2017**, *5*, 11532-11541.	cyano-substituted vinylacridine derivatives	AIE	TFA (DL= 0.5 ppm) HCl (DL= 1.26 ppm) AcOH (DL= 0.12 ppm)	Aniline (DL=0.33 ppb) *N*,*N*-dimethylaniline (DL=1.38 ppb) *N*-methylaniline (DL=0.48 ppb) Phenylhydrazine (DL=3.8 ppb)

2	*Chem. Eur. J.* **2015**, *21*, 4712-4720.	l-phenylalanine derivatives with 5,8-bis(2-(carbazol-3-yl)vinyl)quinoxaline and 5,8-bis[2-(carbazol-3-yl)]-2,3-dimethylquinoxaline	ICT, AIE	TFA (DL= 3.29ppm) TFA (DL= 43 ppb) HCl (DL = 0.122 ppm) AcOH (DL = 0.950 ppm)	
3	*Chem. Eur. J.* **2015**, *21*, 17508-17515.	L-phenylalanine derivative	AIE	TFA (DL= 25 ppb) AcOH (DL= 0.102 ppm) HCl (DL= 0.556 ppm)	Aniline (DL=0.769 ppb) *N*-methylaniline (DL=7.1 ppb) *N*,*N*-dimethylaniline (DL=1.9 ppb)
4	*Chem. Asian J.* **2015**, *10*, 1717 – 1724.	phenanthroimidazole derivatives	AIE	TFA (7.4 ppm)	
5	*New J Chem* **2017**, *41*, 263-270.	Triphenylamine modified benzothiazole derivative	ICT, Piezochro-mism	TFA (DL=2.8 ppm) HCl, HNO_3	
6	*New J Chem* **2018**, *42*, 17524-17532.	9,9-dibutyl-7-(3,5-di(pyridin-2-yl)phenyl)-*N*-(3,4,5-tris(dodecyloxy)-phenyl)-9H-fluorene-2-carboxamide	ICT, AIE	TFA (DL=2.3 ppm) HCOOH, AcOH, HCl, HNO_3	
7	*RSC Adv.* **2016**, *6*, 92144-92151.	phenothiazine modified benzothiazole derivative	ICT, mechanochr omism	TFA (DL= 2.3 ppm) HCl, HNO_3	
8	*J. Mater. Chem. C* **2015**, *3*, 8888-8894.	benzothiazole modified carbazole derivatives	Emission from xerogel film	TFA (DL=1.5ppm) HCl (5.2 ppm), HNO_3, HCOOH, AcOH	
9	*Nano Lett.* **2008**, *8*, 2219-2223.	*N*-(1-hexylheptyl)perylene-3,4,9,10-	Emission from		Aniline (DL=0.2 ppb)

		tetracarboxyl-3,4-anhydride-9,10-imide.	fluorescent nanofibers		
10	*Chem. Commun.* **2013**, *49*, 5838-5840.	*N*-lauroyl phenylalanines and 1,4-bis(2-(pyridin-4-yl)vinyl)benzene based two component gel	Emission from the gel		Aniline (DL=1.8 ppb)
11	*RSC Adv.* **2015**, *5*, 25125-25131.	Trifluoroacetyl substituted anthracene, pyrene and triphenylamine derivatives	Solvatochromism, solid state fluorescence		Aniline (DL=0.23 ppb)
12	*J. Mater. Chem. C* **2017**, *5*, 11781—11789.	salicylaldehyde derivatives functionalized naphthalimides and tert-butyl carbazole	ICT, AIE		Aniline (DL=1.306 ppm)
13	*New J Chem* **2015**, *39*, 6874-6881.	*N*-lauroyl phenylalanines and pyridine substituted styrene based two component gel	Enhanced emission from gel		Aniline (DL=1.6 ppb), *N*,*N*-dimethylaniline, *N*-methylaniline
14	*ChemistrySelect* **2017**, *2*, 2841 – 2846.	Dicyano Oligo (P-Phenylenevinylene)	Emission upon aggregation		Aniline (DL=21 ppb), *N*,*N*-dimethylaniline (DL=11 ppb), *N*-methylaniline (DL=5 ppb)
15	**Present study**	**2-Benzyl-1-(4-methoxyphenyl)-3-phenylindeno[1,2-*c*]pyrrol-8(2*H*)-one**	Solvatochromism, AIE, and solid state emission	TFA (DL=0.77 ppm), HCl (DL=0.088 ppm), HNO_3 (DL=0.38 ppm), AcOH (DL=0.48 ppm)	Aniline (DL=6.04 ppb), *N*,*N*-dimethylaniline (DL=8.82 ppb), *N*-methylaniline (DL=3.24 ppb), Phenylhydrazine (DL=0.16 ppb)

REFERENCES:

1. Santhi, J.; Baire, B. N-Iodosuccinimide-Promoted Rapid Access to Indeno [1, 2-*c*] pyrroles via [3+ 2] Annulation of Enamine-alkynes. *Adv. Synth. Catal.* **2016**, *358*, 3817-3823.

2. Dobelmann, L.; Parham, A.; Büsing, A.; Buchholz, H.; König, B. First Synthesis of Naphthalene Annulated Oxepins. *RSC Adv.* **2014,** *4*, 60473-60477.

3. Afonin, A.; Toryashinova, D. D.; Schmidt, E. Y. Investigation of C–H··· X (X= N, O, S) Intramolecular Hydrogen Bond in 1-vinyl-2-(2′-heteroaryl) pyrroles by ab initio Calculations. *Journal of Molecular Structure (Theochem)* **2004**, *680*, 127-135.

4. Cai, M.; Gao, Z.; Zhou, X.; Wang, X.; Chen, S.; Zhao, Y.; Qian, Y.; Shi, N.; Mi, B.; Xie, L. A Small Change in Molecular Structure, a Big Difference in the AIEE Mechanism. *Phys. Chem. Chem. Phys.* **2012**, *14*, 5289-5296.

5. Lippert, E. Z. Dipole Moment and Electron Structure of Excited Molecules *Naturforsch. A: Phys. Sci.* **1955**, *10*, 541-545.

6. Sivalingam, S.; Debsharma, K.; Dasgupta, A.; Sankararaman, S.; Prasad, E. Effect of Slip-Stack Self-Assembly on Aggregation-Induced Emission and Solid-State Luminescence in 1, 3-Diarylpropynones. *ChemPlusChem* **2019**, *84*, 392-402.

7. Hu, J.; Liu, R.; Zhai, S.; Wu, Y.; Zhang, H.; Cheng, H.; Zhu, H. AIE-Active Molecule-Based Self-Assembled Nano-Fibrous Films for Sensitive Detection of Volatile Organic Amines. *J. Mater. Chem. C* **2017**, *5*, 11781-11789.

8. Pramanik, S.; Deol, H.; Bhalla, V.; Kumar, M. AIEE Active Donor−Acceptor−Donor-Based Hexaphenylbenzene Probe for Recognition of Aliphatic and Aromatic Amines. *ACS Appl. Mater. Interfaces* **2018**, *10*, 12112−12123.

9. Rehm, D.; Weller, A. Kinetics of Fluorescence Quenching by Electron and H-Atom Transfer. *Isr. J. Chem.* **1970**, *8*, 259-271.